Responses to the Reviewer

Retrieval of the thickness of undeformed sea ice from Simulated C-band compact polarimetric SAR images

X. Zhang, and W. Dierking

To the editor and Dr. Kern:

Reviewers' comments are in blue immediately followed by our response (red).

Since this is the revised version of the manuscript I initially reviewed I skip to write a summary here. Instead I comment on the rebuttal letter which the authors wrote in a careful way, replying convincingly to the concerns I had with the previous version of the manuscript.

We would like to thank the reviewer for his thorough and comprehensive analysis of the manuscript and his constructive suggestions.

The manuscript has substantially improved. I have no general concerns anymore but I recommend that the authors spend a little more time in

i) clarifying the apparent differences between their model results - which start at a thickness of around 0.2 m - and the experimental results which show sea ice thickness values down to 0.1 m or even below that. A comment stating that the theory is valid for sea ice thickness values below 0.2 m and also continues in the way as suggested for sea ice thickness values close to that limit would be helpful (Note that the slope e.g. in Figure 5 decreases particularly for the larger incidence angles around 0.2 m, and it is not clear what is the thickness of the very first data point.);

ii) summarizing their results in a more modest way with regard to the uncertainty and with regard to the validity of their approach as a function of the sea ice thickness encountered;

iii) commenting on the obviously peculiar sea ice thickness distribution for the fast ice areas;

iv) using a more correct terminology in terms of ice types related to the thickness range they are considering.

All these points are mentioned again in the specific comments in more detail.

Since the reviewer repeats the recommendations listed here in the specific comments section we prefer to answer below.

General comments:

None

Specific comments:

P1, L17: I am a bit confused about what is meant here with "radar parameters" given the fact that further up you highlight the CP-Ratio.

Thanks, we clarified this

P2, L15: I suggest to replace "thin" by "first-year" or "seasonal" because "thin ice" by WMO definition is sea ice < 30 cm thick and this is not what Kwok et al. referred to in their paper. I suggest to add an "e.g." as well in front of the citation.

Thanks, we did.

P2, L18: Same as above, I suggest to add an "e.g." as well in front of the citation.

Done.

P3, L4: The authors could add "near-real time" to underline the difference between operational applications and climate applications.

Done.

P3, L10: What is "sufficient accuracy"? 1 m? 1 cm?

We specified this.

P4, L5: Why would one convert a PDF of freeboard into a PDF of draft?

The “draft” has been changed to “thickness”.

P4, L19: I am not too happy with this sentence. Space-borne altimeters have been used to map sea ice thickness, yes. But from space-borne radiometers there are only a few attempts to derive sea ice thickness. Most of them - if not all of them - are severely limited concerning the maximum sea ice thickness to be retrieved. Therefore space-borne radiometers should not be mentioned in the context of being a main source of sea ice thickness retrieval.

We followed the reviewer’s suggestion.

P4, L22: I don't think that this sentence reflects the nature of the SMOS sea ice thickness retrieval. I suggest that the authors read the paper by Huntemann et al. (2014) they cited and also the paper by Tian-Kunze et al. (2014, The Cryosphere) to describe properly how sea ice thickness information is retrieved using SMOS data.

We rephrased this part, now not referring to the procedure of the actual ice thickness retrieval (which according to our opinion would be too lengthy for the introduction) but mentioning that passive microwave sensors can be used, considering their limitations.

P5, L4-7: The citations refer to ICESat and CryoSat-2 only. I suggest the authors either remove the other two sensors or they add suitable citations for these other two sensors as well.

Thanks, we have removed the other two sensors.

P5, L9: The authors could add "radar" in front of "altimeters systems" because they omitted ICESat which had a footprint of about 70 m diameter and ICESat-2 which will have footprints of the order of a few meters.

The information about ICESAT was provided.

P6, L11: I suggest to write "A RADARSAT-2 Quad-pol scene ..." instead of "The RADARSAT-2 scene ..."

Done.

P6, L12/13: I suggest to omit the "()" around the information about the swath width.

Done.

P6, L14-16: Perhaps the authors could underline this statement with a citation?

Done.

P10, L17: Perhaps better "We consider the CTLR ..."?

Done.

P20, L17/18: The authors could switch the two last elements in this sentence: "... of brine inclusions reduces due to desalination processes as ice thickness increases."

Done.

Figure 6: What is the motivation to use case 2 (light nilas) here instead of case 3 as is used in Figure 5? Is this to demonstrate the sensitivity (change) for even smoother sea ice than case 3 sea ice?

Yes.

P21, L16-19 / Figure 7: I have difficulties to understand what the authors say here. The sensitivity of the CP-Ratio to sea ice thickness does not change as function of incidence angle; only the magnitude of the CP-ratio changes. Now: Why is it better to have a high CP-Ratio? Figure 7 reveals that for thin ice (0.2 m) the sensitivity is larger at smaller (20 degrees) than larger (60 degrees) incidence angle.

We rephrased the text to make clear that the incidence angle change causes a change in magnitude of the CPR but does hardly change the sensitivity (which is represented

by the local slope of the curve)

Figure 7 starts at 0.2 m but includes annotations for DN and LN, which are both sea ice types with a maximum sea ice thickness below 0.2 m. My understanding so far was that DN is something until about 5 cm while LN goes until 10 cm continued by grey ice and grey-white ice.

We rephrased this, avoiding the link between roughness and ice type. See also page 20 top, reference to Onstott and list of roughness values.

P21, L22: Yes, that is true - at least down to sea ice thickness values of about 0.2 m.

See above.

P22, L6/7: The sentence: "This regime ..." reads as if the sea ice thickness retrieval would only be possible for the range 0.2 to 0.4 m - which is not the case I assume.

Yes, that is right. We modified the text and give a hint to the experimental results that are discussed later.

P24, L14/15: I guess the authors meant "... overlain with the EMS flight tracks ..." because I cannot see any sea ice thickness information on Figure 8, bottom.

We considered this.

P24, L20: I suggest to replace "several open water and scattered frazil ice areas" by "several openings" because I doubt that the authors can make a statement about which is open water, which is dark nilas, and which is frazil ice.

We considered this.

P25, L3/4: May I ask at which air temperatures this heavy snow fall was reported? And what is "heavy"? 10 inches of snow?

The average air temperature was provided. However, we did not find the information about the snow thickness.

	Temp °C	Dew Point Temp °C	Rel Hum %	Wind Dir 10's deg	Wind Spd km/h	Visibility km	Stn Press kPa	Hmdx	Wind Chill	Weather
TIME										
00:00										
01:00										
02:00										
03:00										
04:00										

05:00	-11.8	-13.7	86	25	39	3.2	99.21	-23	Snow
06:00	-12.0	-13.4	89	24	43	0.8	99.22	-24	Snow,Blowing Snow
07:00	-10.2	-11.4	91	24	28	0.8	99.16	-19	Snow,Blowing Snow
08:00	-5.6	-6.3	95	34	44	0.8	99.20	-15	Snow,Blowing Snow
09:00	-5.5	-6.2	95	33	57	0.8	99.29	-16	Snow,Blowing Snow
10:00	-5.8	-6.5	95	34	52	0.8	99.46	-16	Snow,Blowing Snow
11:00	-7.0	-7.9	93	34	65	0.8	99.64	-19	Snow,Blowing Snow
12:00	-7.4	-8.3	93	34	46	0.8	99.81	-18	Snow,Blowing Snow
13:00	-10.2	-11.8	88	34	52	2.4	99.93	-22	Snow
14:00	-9.7	-11.3	88	33	48	2.4	99.98	-21	Snow
15:00	-10.5	-12.2	87	32	26	4.8	100.14	-20	Snow
16:00	-10.5	-12.6	85	32	26	4.8	100.24	-20	Snow

P25, L5: I suggest to add "(not shown)" behind "... photos."

Done.

P25, L7-10: The authors may be right here with their statement but i) the study of Barber and Nghiem was based on mostly fast ice within the Canadian Arctic Archipelago which grows under different environmental conditions and ii) the fact

that heavy snow fall was reported for 2-3 days beforehand could be an indication that the snow load may easily have been able to reduce the elevation of the ice-snow interfaces towards - if not even below - the water line. This could cause sea water entering the ice-snow interface and being wicked up also at air temperatures below -20 degree C. But at the end this might not be that relevant for this first case study.

Yes, we agree. However, we note that some of our data were taken over fast ice (even though at a different region), and the histograms shown in Fig. 9 indicate that it is not very likely that larger areas are flooded (and only in this case sea water can be wicked up). Nevertheless, we mention the possibility of flooding in our text.

P25, L12-15 / Figure 9:

- I suggest to add the bin width in the caption of Figure 9.

Done

- I suggest further to mention which flight tracks are used to generate which histogram. The information is given on P26 but I suggest to place it closer to Figure 9.

The information is now provided in the figure caption.

- I find it a bit peculiar that the fast ice total ice thickness histogram has these multiple modes. In particular, the modal sea ice thickness is located at the bin centered at 20 cm (which seems odd in March, close to the end of the sea ice growth season), there is a second mode centered at 80 cm and a shoulder extending to about 190 cm. The authors could have commented on this.

We did not regard the second local maximum as a significant mode. Even at the end of the ice season cold periods may occur so that new ice forms and grows.

- The authors mention in L14 that "it" consists of rafted floes. How do they know? Is this the interpretation of the total ice thickness histograms?

This was an error – we removed this part of the sentence.

- L15: "reveals a deeper snow cover". Well, yes and no. The modal snow depth is 6 cm in both cases - but indeed the landfast ice has a second mode at about 15 cm which is missing for the drift ice. However, since the critical snow depth in your investigation is something like 20 cm you could perhaps give the percentage of data

with snow depths below / above your "critical" snow depth.

The information is now provided in the text.

P27, L8-10: Does this mean that you excluded deformed ice from you analysis as well? It gets not clear in what the authors write here. I can formulate the question also like this: Are areas with deformed ice in the SAR image still entering step 5 or not?

Please noted that the deformed ice was excluded by visual interpretation as mentioned at the end of section 4.2. We expect the most deformed ice area are excluded in step 4.

P27, L13: "ice zones of 50 m in length"? Are the authors talking about the co-located, drift-corrected EMS tracks in the SAR image? Perhaps the authors could use here also "segment" or "flight track segment"? The authors could write more clearly that the flight tracks were cut into 50 m long segments. For these segments simulated CP SAR data were taken from the co-located, drift-corrected, segmented SAR images - provided that the 50 m segment contains a homogeneous piece of ice.

We modified the text accordingly, although not in 1:1 correspondence to the reviewer's wording

- What is the motivation to use 50 m?

We explained this more in detail.

P27, L19: Could it be that the 13 × 13 pixel window was chosen in accordance with the lee-filter used in the pre-processing?

Yes, see text and our answer above.

P28, L21: Could be, yes, but we have seen that the used parametrization is sub-optimal at around 0.4 m sea ice thickness and creates an inconsistency.

We guess the reviewer talks about the salinity "parameterization". We mention this also in the text now.

Figure 10:

- If I compare Figure 10 with Figure 5-7 I can see that the measurements end up at a smaller CP-ratio than the theoretical computations. The authors could comment on this in the paper - i.e. that this is not relevant and to be expected as the model underlying the theoretical calculations was an over-simplication of the actual situation.

We considered this in the text.

- I like the 90% confidence intervals of the fitted lines. It is, however, nice to see that there are hardly any CP-ratio values below 0.03 (except one). Could this be taken as sort of an uncertainty range for the CP-ratio derived from SAR? How accurate can you (theoretically) estimate - with your current knowledge about the accuracy of the used RADARSAT-2 SAR data - the CP-ratio? I am asking because in P29, L10, you set the upper limit to 1.8 m and I am wondering what the motivation for this upper limit is?

The idea for using thickness values up to 1.8 m was that the larger ice thicknesses can be measured with a higher accuracy, which makes the fit more robust. However, the accuracy of the CP-ratio is difficult to judge since no distributions due to speckle has been derived yet (to our knowledge).

- The authors state on P29, L9, that all data points (320 samples) are used. Am I correct assuming that this is the entire number of data points shown in Figure 10?

Yes, all data points are shown in Fig. 10.

I am wondering whether the authors could make a comment - if deemed relevant - about the fact that for incidence angle 49 degrees they could use almost only (except 1) sea ice thickness values > 0.5 m.

We did this.

- The ice thickness shown here (and in Figure 11) is the total (ice + snow) thickness minust the snow depth, right?

Yes, we have mentioned it in Section 4.2.

P29, L10: While I see that your measurements went all the way down to even less than 0.1 m, in your theory you did not go down to these low sea ice thickness values.

Figure 5-7 stop at about 0.2 m and do (by the way) not suggest a further increase in the sensitivity to sea ice thickness as indicated in Figure 10. Is this a limitation of the theory?

We think yes – because of the over-simplification of the model (see comment above). When calculating the CPR, oscillations occur for ice thicknesses < 0.16 m, which we attribute to possible interactions between ice surface and ice-water interface in the volume scattering model. We mention this at the end of section 3.

P30, L2: The authors could add that the division of the 159 samples into two sub-samples was done in an arbitrary way.

We considered this.

P30, L6: The authors could add that these coefficients are (of course) different from those derived in Eq. (14) from the same two SAR images.

We considered this.

P30, L12/13: I am not sure what the authors wish to stress with the sentence put in (...) here. The latter case are the smaller sea ice thickness values.

We have removed the sentence.

P30, L14-17: I like this statement. It can be also seen from Figure 11 a) that until CP-ratios of 0.08 the sea ice thickness range retrieved is relatively small whereas - at least in the example shown - for CP-ratios < 0.08 the range of retrieved sea ice thickness values increases a lot. In a way your example suggests a "saturation" thickness of between 0.6 m and 0.8 m to be retrieved with the CP-ratio with reasonable accuracy. This is also supported by the break in the good relationship between estimated and observed sea ice thickness between 0.6 m and 0.8 m shown in Figure 11 b).

Yes

Figure 11, Caption, L5: What is meant by "standard deviation of the plots"?

Done.

P31, L7-10: I suggest to the authors (following up with my comment just above) that they are even more careful in making statements about the sea ice thickness range and the accuracy with which the sea ice thickness can be retrieved from the CP-ratio with their method. Figure 11 clearly reveals that the relationship between CP-ratio and sea ice thickness potentially breaks down above a sea ice thickness of about 0.6 m to 0.8 m - at least for the sea ice encountered in their area of interest. Stating that the RMS error is 0.12 m for the range 0.1 - 1.8 m is a bit misleading seeing the fraction of data points with sea ice thickness > 0.7 m; only 8 data points are above 0.7 m which is 1/10 of the number of samples shown in Figure 11a). Hence the low RMS-error for the large range is dominated by the RMS of the other 90% of the data which are at sea ice thickness < 0.7 m.

In addition to that, in order to obtain the sea ice thickness values shown in Figures 10 and 11 you needed to discarded regions of deformed sea ice from the SAR images as described in section 4.2. How likely is it that the relatively few remaining thick sea ice cases are in fact not level thick sea ice but also originate from deformation events?

The histograms of the total (ice + snow) thickness reveal dominant modes at around 0.5 m and around 0.8 m for drift ice and fast ice, respectively, which points to that likely these are the "typical" total thickness values observed - in addition to the yet unexplained 1st fast ice thickness mode at 0.2 m.

Therefore, in the light of the above-said and in the light of the environmental conditions I would be "honest" and state perhaps the range 0.1 m to 0.8 m as the most useful range for your application at the current stage.

We have considered these.

P31, L11: I suggest to replace "is" by "can be".

We did.

Typos:

P3, L2: "e. g." --> "e.g."

Done.

P10, L11: "conisdering" --> "considering"

Done.

Figure 4: Legend and y-axis annotation says "The volumes fraction ..." Shouldn't it be "The volume fraction ..."?

Done.

The authors might check whether "CP-Ratio" is written in italic font in the running text. They might also check whether they always wrote "CP-Ratio" and not just "CP" (for the latter see P21, L15).

Done.

P23, L12: "G Hz" --> "GHz"

Done.

P24, L15: "According the" --> "According to the"

Done.

P28, L21: Delete "since"

Done.

Retrieval of the thickness of undeformed sea ice from Simulated C-band compact polarimetric SAR images

X. Zhang[1], W. Dierking[2], J. Zhang[1], J. M. Meng[1], and H. T. Lang[3]

[1]{the First Institute of Oceanography, State Oceanic Administration, Qingdao, China}

[2]{Alfred Wegener Institute for Polar and Marine Research, Bremerhaven, Germany}

[3]{Beijing University of Chemical Technology, Beijing, China}

Correspondence to: X. Zhang (zhangxi1981@gmail.com)

Abstract. In this paper we introduce a parameter for the retrieval of the thickness of undeformed first-year sea ice that is specifically adapted to compact polarimetric (CP) synthetic aperture radar (SAR) images. The parameter is denoted as "*CP-Ratio*". In model simulations we investigated the sensitivity of *CP-Ratio* to the dielectric constant, ice thickness, ice surface roughness, and radar incidence angle. From the results of the simulations we deduced optimal sea ice conditions and radar incidence angles for the ice thickness retrieval. C-band SAR data acquired over the Labrador Sea in circular transmit, linear receive (CTLR) mode were generated from RADARSAT-2 quad-polarization images. In comparison with results from helicopter-borne measurements we tested different empirical equations for the retrieval of ice thickness. An exponential fit between *CP-Ratio* and ice thickness provides the most reliable results. Based on a validation using other compact polarimetric SAR images from the same region we found a root mean square (rms) error of 8 cm and a maximum correlation coefficient of 0.94 for the retrieval procedure when applying it to level ice between 0.1 m and 0.8 m thick.

删除的内容: parameters

删除的内容: 12

删除的内容: 93

删除的内容: 1

1 Introduction

Sea ice covers about one tenth of the world ocean surface and significantly affects the exchanges of momentum, heat, and mass between the sea and the atmosphere. Not only sea ice extent is a significant indicator and effective modulator of regional and global climate change, but also sea ice thickness is an important parameter from a thermodynamic and kinematic perspective (Soulis et al., 1989; Kwok, 2010). The decline of sea ice extent recently observed in the Arctic, e. g. is linked with a decrease of ice thickness and increasing fractions of seasonal ice areas (e.g. Kwok et al., 2009). Measurements of sea ice thickness are compared with model results to control and validate the model capabilities for reproducing recent and predicting future trends of sea ice conditions in the Arctic (e.g. Laxon et al., 2013). Although sea ice thickness is only several meters at most, it forms an effective thermal insulation layer due to its high albedo and low thermal conductivity, leading to a significant reduction in the heat flux from the ocean to the atmosphere, especially in winter (Vancoppenolle et al., 2005). Besides investigations focusing on the entire Arctic or Antarctic region, other studies analyze ice thickness variations on local scales to improve regional ice thickness retrievals (e.g. Haapala et al., 2013). Operational services charged with providing sea ice maps and forecasting ice conditions for marine transportation and offshore operations need near-real time regular information about local and regional ice thickness distributions. The use of sensors providing high spatial resolutions on the order of 100 meters or better such as SAR for ice thickness retrieval is an important topic of recent research (Dierking, 2013).

Unfortunately, the sea ice thickness distribution is also one of the most difficult parameter to measure. The most direct and accurate measurement technique is in-situ drilling with an ice auger. Although it provides data with sufficient accuracy (in the range of centimeters), it is time consuming and spatially limited. Therefore, this method is used mainly for calibration of other sensors or methods. To obtain ice thickness distributions at larger spatial scales, remote sensing methods are requisite tools. There are generally different strategies:

1) Measurements of ice draft using upward-looking sonar on ocean moorings or

删除的内容: thin

删除的内容:

删除的内容: ,

submarines (Wadhams, 1980; Behrendt et al., 2013) from which thickness is estimated based on assumptions about buoyancy, ice density, and snow load (e. g. Rothrock et al., 1999). Such data provide information about detailed temporal thickness variations (daily or even hourly) at a fixed location. An example for using in situ measurements of ice thickness from the New Arctic Program initiated by the Canadian Ice Service (CIS) starting in 2002, and sea ice draft measurements from moored ULS instruments in the Beaufort Gyre Observing System for testing a method of ice thickness retrieval from optical methods is provided by Wang et al. (2010).

2) Measurements of sea ice freeboard (i.e., the part of the ice above the water level) plus snow layer thickness with laser altimetry (e. g. Wadhams et al., 1992; Dierking, 1995). From such data, the average ice thickness can be estimated, or the probability density function (PDF) of ice freeboard can be converted to a PDF of ice thickness. However, the estimation of ice thickness from freeboard data is less reliable than from ice draft because of a relatively stronger impact of errors in the freeboard measurements (Goebell, 2011).

3) Measuring the distance between snow surface and ice bottom with electromagnetic induction sounders (EMS) mounted on sledges, ships or helicopters/airplanes (Goebell, 2011; Haas et al., 1997; Prinsenberg et al., 2012a, 2012b). With such systems, spatial ice thickness variations measured at horizontal distances of a few 10 meters were obtained in various regions (Kovacs et al., 1987; Rossiter and Holladay, 1994; Haas et al., 2006; Hendricks et al. 2011).

Although ULS and EMS have all contributed greatly to our knowledge about ice thickness distributions on local and regional scales, such data can be obtained only at specific locations over a limited time period. Satellite remote sensing, on the other hand, is useful to monitor ice thickness variations regularly over much larger areas.

On a still experimental basis, data of L-band passive microwave sensors, such as for example the Soil Moisture and Ocean Salinity mission (SMOS) radiometer, have been employed to retrieve thickness of sea-ice thinner than about half a meter. The limitation of this approach is that it is only possible for very high (almost 100%) sea ice concentration and in cold freezing conditions (Tian-Kunze et al., 2014;

删除的内容: draft

删除的内容: Space-borne radiometer and altimeter hasve been used primarily to map ice thickness, and to monitor and study their trends.

删除的内容: In case

删除的内容: the difference between horizontally and vertically polarized emission is correlated with sea-ice

删除的内容: .

删除的内容: ice thickness retrieval using

删除的内容: type of sensor

带格式的: 字体颜色：文字 1

删除的内容: Kaleschke

带格式的: 字体颜色：文字 1

删除的内容: 2

Huntemann et al., 2014). Space-borne altimeter has been used primarily to map ice thickness, and to monitor and study their trends. The capabilities of laser and radar altimeter systems (such as CryoSat-2 and ICESAT) for measuring ice freeboard have been extensively investigated during the last decade (e. g. Kwok and Cunningham, 2008; Kwok et al., 2009; Laxon et al., 2013). Compared with radiometers, which collect data only at a coarse spatial resolution of a few to tens of kilometers (e.g. 25 km for SSM/I 37 GHz data), the spatial resolutions of radar altimeter systems are about 250 m along-track for CryoSat-2, and a footprint of about 70 m diameter for ICESAT. The sea ice products derived from altimeters usually focus on large-scale spatial and temporal variations. While the large-scale ice thickness product is important for climate research, the support of marine navigation and offshore operations in polar areas are crucially dependent on precise and reliable sea ice thickness maps with spatial resolutions better than 1 km.

Space-borne synthetic aperture radar (SAR), which operates in the microwave frequency band, provides all-weather and day-night high-resolution imagery (within a range of 1-100 m) with 1~3 days' temporal coverage. Hence, SAR is in general very useful for operational mapping tasks on regional and local spatial scales (Dierking, 2013). The disadvantage of SAR systems is that higher spatial resolutions are linked with a limited coverage between 10 and 500 km, compared for example to more than 1000 km for passive microwave radiometers. SAR measures the intensity of the radar signal backscattered from the ice surface and volume at different polarizations. The backscattered intensity depends on the dielectric constant of the ice and small-scale (mm – dm range) ice properties such as ice surface roughness and air bubble fractions and sizes. If at least two polarizations are measured simultaneously, the SAR, which is a coherent device, can also provide the phase difference between the differently polarized channels. The most recent SAR sensors have polarimetric capabilities. A fully polarimetric radar transmits and receives both linear horizontal (H) and vertical (V) polarized electromagnetic waves. Amplitude and phase information of the backscattered signal are recorded for four transmit/receive polarizations (HH, HV, VH and VV). This mode is commonly referred to as "quad-pol". Quad-pol scenes are

删除的内容: ENVISAT radar altimeter, ERS-1/2 radar altimeter,

删除的内容: higher:

删除的内容: 5 km for the ENVISAT radar altimeter, and 1.2 km across-track,

删除的内容: .

删除的内容: radiometers and

删除的内容:

usually acquired at very high spatial resolution. A RADARSAT-2 Quad-pol scene has a spatial resolution of 4.7 m (slant range) × 5.0 m (azimuth) at a swath width of 25/50 km. Dual-pol scenes contain two polarimetric channels (e.g. HH and HV or VV and VH). In operational ice-charting services dual-pol scenes are preferred because of their wider areal coverage (Geldsetzer et al., 2015). The RADARSAT-2 ScanSAR Wide mode, e.g., can have a swath width of 500 km with 160-72 m (ground range) × 100 m (azimuth) resolution. Despite their currently very limited coverage, the quad-pol images are important information sources to understand the scattering mechanisms of sea ice.

Recently a number of investigators noted correlations between ice thickness and the co-polarization ratio, which is the ratio of measured intensities at VV- and HH-polarization (here we use VV/HH). The sensitivity between co-polarization ratio and thin ice thickness has been firstly demonstrated by Onstott (1992), based on C-band radar data from the Eastern Arctic region. Kwok et al. (1995) estimated the thin ice thickness (0 to 0.1m) from L- and C- band fully polarimetric airborne SAR data acquired over the Beaufort Sea. Their approach included the training of a neural network. L-band polarimetric characteristics of ice in the Sea of Okhotsk were investigated by Wakabayashi et al. (2004), and the L-band co-polarized ratio was used to estimate ice thicknesses between 0 and 2 m (their Fig. 13). The investigation was further extended to other sensors, e.g. to the airborne Pi-SAR (X-, and L-band, data from the Sea of Okhotsk; Nakamura et al., 2009a; Toyota et al., 2009) and to ENVISAT ASAR, using radar intensity and ice thickness data from 0.2 to 2.5 m, the latter acquired from a research vessel in the Lützow-Holm Bay Antarctica (Nakamura et al., 2009b). The good correlations were attributed to the fact that the co-polarized ratio values are sensitive to the dielectric constants of the ice surface layer which changes due to the process of desalination during ice growth. The relationship between relatively thick multi-year ice (thickness between 2 m and 5 m), on the one hand, and co-polarized correlation and cross-polarized ratio HV/HH or VH/VV, on the other hand, was also investigated in the Arctic Ocean employing RADARSAT-2 and TERRASAR-X data (Kim et al., 2012). They found that the degree of

删除的内容: The

删除的内容: (

删除的内容:).

删除的内容: , e.g. the

depolarization is linked to the thickness of the MYI as ice surface roughness increases and salinity decreases.

Although the above mentioned parameters derived from polarimetric SAR imagery have shown the potential for estimating sea-ice thickness under certain conditions, polarimetric SAR data can presently only be acquired at limited swath-widths. The quad-pol mode on RADARSAT-2, has a swath width of only 25-50 km, as mentioned above. The swath width of the VV/HH dual-polarization Stripmap mode on TerraSAR-X is 15 km. Therefore, they are insufficient for operational use which requires a large-scale coverage (Scheuchl et al., 2004). The limited swath-width also restricts scientific investigations to local domains. An alternative is to use compact polarimetry.

The methods of generating compact polarimetric (CP) information (explained below) are based on receiving data at two different polarizations (Souyris et al., 2005; Raney, 2007). Compared with the "traditional" dual-polarization modes described above, CP data include a greater amount of polarization information (but less than quad-polarization data). They can cover much greater swath widths compared to quad-polarization modes due to reduced power consumption and data storage requirements.

The term "CP system" refers to a unique polarization in transmission and coherent dual-orthogonal polarizations in reception. There are three different CP configurations (Nord et al., 2009). The first architecture is the "$\pi/4$ mode" with a slant linear transmission and horizontal (H) and vertical (V) receptions (Souyris et al., 2005). The second is the "dual circular (DC) mode", i.e. transmitting at a single circular polarization and receiving two orthogonal circular polarizations. The last approach is circular transmit and linear (H and V) receive (called CTLR mode). Among these three compact polarization modes, the latter has been ranked to be the most promising in terms of performance and receiver complexity. The current Indian RISAT-1, the Japanese ALOS-2 and the planned Canadian RADARSAT Constellation Mission (RCM) also support the CTLR mode. According to the description in Geldsetzer et al. (2015), the coming CTLR mode of RCM will be particularly tailored to sea ice

applications by offering a medium-resolution mode with a swath width of 350 km and a resolution of 50 m, a low-noise mode with the same swath width and a resolution of 100 m., or a low-resolution mode with a swath width of 500 km and a resolution of 100 m. Hence, the CTLR modes of RCM are well suited for operational sea ice monitoring.

However, one apparent disadvantage of the CP mode as compared to dual- or quad-polarization mode is the fact that the HH, VV, and HV signal combinations are not directly measured. This means that the co-polarized ratio (Wakabayashi et al., 2004; Nakamura et al., 2009a; Toyota et al., 2009) and the cross-polarized ratio (Kim et al., 2012) which are often used as an ice thickness proxy cannot be directly calculated from CP mode SAR data. Although CP SAR images have been used to distinguish sea ice types (Dabboor and Geldsetzer, 2014; Charbonneau et al., 2010; Geldsetzer et al., 2015), to our knowledge there have been no published studies on its use for ice-thickness detection in the open literature until now. Therefore, in this study, we considered the CTLR mode and developed an approach to directly retrieve the thickness from CP SAR data (hereafter we assume that the CP SAR is operated in CTLR mode). The paper is organized as follows: in Sect. 2 we introduce a new parameter to estimate ice-thickness and demonstrate its sensitivity to different ice parameters by numerical modeling in Sect. 3. In Sect. 4, an empirical relationship based on a comparison of CP-SAR signatures with ice thickness data obtained from electromagnetic induction sounding is presented, and the retrieval performance of this algorithm is described. Further discussions and conclusion are presented in Sect. 5.

2 Model and method

2.1 Full polarimetry and compact polarimetry

The full polarimetric radar scattering return can be represented by the scattering matrix **S**

$$S = \begin{bmatrix} S_{HH} & S_{HV} \\ S_{VH} & S_{VV} \end{bmatrix} \quad (1)$$

where S_{pq} denotes the p transmit and q received linear polarization. In the monostatic case and considering that reciprocity can be assumed for sea ice and snow, $S_{HV}=S_{VH}$. We use the coherency matrix **T** to evaluate the second-order statistics of the scattering matrix **S**. The coherency matrix **T** formed from the elements of the scattering matrix **S** is

$$T = \frac{1}{2}\begin{bmatrix} \left\langle |S_{HH}+S_{VV}|^2 \right\rangle & \left\langle (S_{HH}+S_{VV})(S_{HH}-S_{VV})^* \right\rangle & 2\left\langle (S_{HH}+S_{VV})S_{HV}^* \right\rangle \\ \left\langle (S_{HH}-S_{VV})(S_{HH}+S_{VV})^* \right\rangle & \left\langle |S_{HH}-S_{VV}|^2 \right\rangle & 2\left\langle (S_{HH}-S_{VV})S_{HV}^* \right\rangle \\ 2\left\langle S_{HV}(S_{HH}+S_{VV})^* \right\rangle & 2\left\langle S_{HV}(S_{HH}-S_{VV})^* \right\rangle & 4\left\langle |S_{HV}|^2 \right\rangle \end{bmatrix} \quad (2)$$

where * denotes the complex conjugate and <•> the ensemble average.

We consider the CTLR mode for which the scattering vectors are given by (e. g. Nord et al, 2009)

$$\vec{k}_{CTLR} = [S_{RH} \quad S_{RV}]^T = [S_{HH} - iS_{HV} \quad -iS_{VV} + S_{HV}]^T / \sqrt{2}\,. \quad (3)$$

As usual, the "*R*" denotes that the transmitted polarization is right circular, while "*H*" and "*V*" stand for the linear reception. We set

$$\Sigma_H = S_{RH} + iS_{RV} \qquad \Sigma_V = S_{RH} - iS_{RV}, \quad (4)$$

From Eq. (3) it then follows that

$$\Sigma_H = S_{HH} + S_{VV} \qquad \Sigma_V = S_{HH} - S_{VV} - i2S_{HV}\,. \quad (5)$$

The terms $\left\langle |\Sigma_H|^2 \right\rangle$ and $\left\langle |\Sigma_V|^2 \right\rangle$ can be expressed as

$$\left\langle |\Sigma_H|^2 \right\rangle = \left\langle (S_{HH}+S_{VV})(S_{HH}+S_{VV})^* \right\rangle = \left\langle |S_{HH}+S_{VV}|^2 \right\rangle,$$

$$\begin{aligned} \left\langle |\Sigma_V|^2 \right\rangle &= \left\langle (S_{HH}-S_{VV}-i2S_{HV})(S_{HH}-S_{VV}-i2S_{HV})^* \right\rangle \\ &= \left\langle (S_{HH}-S_{VV})(S_{HH}-S_{VV})^* \right\rangle + \left\langle i2S_{HV}^*(S_{HH}-S_{VV}) \right\rangle - \left\langle i2S_{HV}(S_{HH}-S_{VV})^* \right\rangle + 4|S_{HV}|^2\,. \\ &= \left\langle |S_{HH}-S_{VV}|^2 \right\rangle + \left\langle i2S_{HV}^*(S_{HH}-S_{VV}) \right\rangle - \left\langle i2S_{HV}(S_{HH}-S_{VV})^* \right\rangle + 4|S_{HV}|^2 \end{aligned} \quad (6)$$

Under the assumption of reflection symmetry, the cross- and co-polarized scattering coefficients are uncorrelated. This assumption is reasonable for snow and sea ice surfaces at various frequencies and for different spatial scales (Souyris et al., 2005).

删除的内容: s

删除的内容: Consider

Hence

$$\left\langle S_{HV}^{*} S_{VV} \right\rangle = \left\langle S_{HH} S_{HV}^{*} \right\rangle \approx 0. \tag{7}$$

and Eq. (6) can be rewritten by the elements of coherency matrix **T**:

$$\left\langle \left| \Sigma_H \right|^2 \right\rangle = \left\langle \left| S_{HH} + S_{VV} \right|^2 \right\rangle = t_{11} \qquad \left\langle \left| \Sigma_V \right|^2 \right\rangle = \left\langle \left| S_{HH} - S_{VV} \right|^2 \right\rangle + 4\left| S_{HV} \right|^2 = t_{22} + t_{33}. \tag{8}$$

2.2 X-Bragg model and X-SPM model

According to the results obtained by the Cold Region Research and Engineering Laboratory (CRREL'88), the typical ranges of RMS height and correlation lengths for smooth level sea ice are 0.02~0.143 cm and 0.669~1.77 cm respectively (Fung, 1994). For C-band SAR, the small perturbation method (SPM) can be applied for explaining the surface scattering characteristics from smooth level sea ice. By doing so the underlying assumption is that the received radar signatures are typical for Bragg scattering. However, the SPM fails to describe cross-polarization and de-polarization effects that are observed in real SAR data. In order to overcome these limitations and to widen the SPM range of validity, an extended Bragg model (termed X-Bragg model) was presented by Hajnsek et al. (2003). In the X-Bragg model the scattering surface is composed of rough randomly tilted facets that are large with respect to the wavelength but small with respect to the spatial resolution of the sensor (for RADARSAT-2 fine-quad mode, the wavelength is 5.6 cm and the resolution is 8 or 25 m). Scattering from each rough facet is evaluated by employing the SPM, whereby for the facets a random tilt is assumed which causes both a random variation $\Delta\theta$ of the incidence angle θ and a random rotation β of the local incidence plane around the line of sight. In the X-Bragg model, the random incidence angle variation $\Delta\theta$ is ignored, and the incidence plane angle of rotation β is assumed to be uniformly distributed in an interval $(-\beta_1, \beta_1)$, where the parameter β_1 is used to characterize the large-scale roughness (del Monaco et al., 2009).

In order to improve the range of validity of the X-Bragg model, different approaches (termed X-SPM model) were proposed by del Monaco et al. (2009) and Iodice et al. (2011). In those studies, more realistic distributions of β and $\Delta\theta$ were derived by

assuming that the range and azimuth facet slopes are Gaussian random variables. The coherency matrix of the X-SPM model ($\mathbf{T}_{X\text{-}SPM}$) after ensemble averaging over the local incidence angle θ_l and rotation angle β can be expressed as follows (del Monaco et al., 2009)

$$T_{X-SPM} = \rho \begin{bmatrix} \left\langle \left|R_S + R_P\right|^2 \right\rangle_{|\theta_l} & c_2 \left\langle (R_S - R_P)(R_S + R_P)^* \right\rangle_{|\theta_l} & 0 \\ c_2 \left\langle (R_S + R_P)(R_P - R_S)^* \right\rangle_{|\theta_l} & cc_2 \left\langle \left|R_S - R_P\right|^2 \right\rangle_{|\theta_l} & 0 \\ 0 & 0 & ss_2 \left\langle \left|R_S - R_P\right|^2 \right\rangle_{|\theta_l} \end{bmatrix}, \quad (9)$$

$$c_2 = \left\langle \cos 2\beta \right\rangle_{|\beta} = -1 + 2cc,$$

$$cc_2 = \left\langle \cos^2 2\beta \right\rangle_{|\beta} = \frac{\sin^2\theta}{\sigma^2} + (1 - 2cc)\frac{\sin^2\theta + \sigma^2}{\sigma^2},$$

$$cc = \left\langle \cos^2 \beta \right\rangle_{|\beta} = \sqrt{\frac{\pi \sin^2\theta}{2\sigma^2}} \exp\left\{\frac{\sin^2\theta}{2\sigma^2}\right\} Erfc\left\{\sqrt{\frac{\sin^2\theta}{2\sigma^2}}\right\},$$

$$ss_2 = \left\langle \sin^2 2\beta \right\rangle_{|\beta} = 1 - cc_2.$$

Here, $\langle\rangle_{\theta_l}$ means averaging over the local incidence angle; θ_l which is used to characterize the random slope variations of the facets; $\langle\rangle_{|\beta}$ means averaging over the rotation angle β; ρ includes small scale roughness effects, and σ is the standard deviation of the surface slope which is a Gaussian random variable. $Erfc\{\bullet\}$ is the complementary Gauss error function. R_P and R_S are the Bragg scattering coefficients perpendicular and parallel to the incident plane, respectively. Both are functions of the complex permittivity ε and the incidence angle θ (Iodice et al., 2011)

$$R_S = \frac{\cos\theta - \sqrt{\varepsilon - \sin^2\theta}}{\cos\theta + \sqrt{\varepsilon - \sin^2\theta}} \qquad R_P = \frac{(\varepsilon - 1)\left[\sin^2\theta - \varepsilon(1 + \sin^2\theta)\right]}{(\varepsilon\cos\theta + \sqrt{\varepsilon - \sin^2\theta})^2}. \quad (10)$$

In the paper by del Monaco et al. (2009) it is demonstrated that the X-SPM model coincides with the X-Bragg model when the standard deviation of the surface slope is zero, and that the X-Bragg model can only be applied for standard deviations of the surface slope $\sigma < 0.1$. When $\sigma > 0.1$, the effects of incidence angle fluctuations, which is ignored in the X-Bragg model, is significant (del Monaco et al., 2009). Because of its wider range of validity, we used the X-SPM model in our study.

2.3 Inversion model

For ice thickness retrievals we propose to exploit the ratio between $\langle|\Sigma_V|^2\rangle$ and $\langle|\Sigma_H|^2\rangle$ (here denoted as the *CP-Ratio*). The *CP-Ratio* can be written as (see Eq. 4)

$$CP-Ratio=\frac{\langle|\Sigma_V|^2\rangle}{\langle|\Sigma_H|^2\rangle}=\frac{\langle|S_{RH}-iS_{RV}|^2\rangle}{\langle|S_{RH}+iS_{RV}|^2\rangle}. \quad (11)$$

By relating the *CP-Ratio* to the elements of the coherency matrix given for the X-SPM we obtain

$$CP-Ratio=\frac{\langle|\Sigma_V|^2\rangle}{\langle|\Sigma_H|^2\rangle}=\frac{cc_2\langle|R_S-R_P|^2\rangle_{|\theta_I}+ss_2\langle|R_S-R_P|^2\rangle_{|\theta_I}}{\langle|R_S+R_P|^2\rangle_{|\theta_I}}=\frac{\langle|R_S-R_P|^2\rangle_{|\theta_I}}{\langle|R_S+R_P|^2\rangle_{|\theta_I}}. \quad (12)$$

Equation (12) shows that the *CP-Ratio* is controlled by ensemble averages of the difference and sum of the Bragg coefficients with respect to the incidence angle. From del Monaco et al. (2009), the probability density function for $\cos\theta_I$ is a normal distribution with mean $\cos\theta$ and standard deviation equal to $\sigma\sin\theta$. After averaging over variations of the local incidence angle θ_I, the *CP-Ratio* is dependent on the dielectric constant of the surface ε, the incidence angle θ, and the standard deviation of the surface slope σ. By using the model of del Monaco et al. (2009), the results of SAR measurements can be better explained than with the SPM.

We calculated the *CP-Ratio* as a function of the standard deviation of surface slope σ assuming ε=3.9+j0.15 which are suggested in (Fung and Eom, 1982) for first year sea ice. The results show that the *CP-Ratio* increases with increasing standard deviation of the surface slope at fixed incidence angles and with increasing incidence angle at fixed σ (Fig. 1). The relationship between *CP-Ratio* and the dielectric constant is presented in Fig. 2. When the incidence angle is constant, the *CP-Ratio* reveals monotonically increasing values with increasing dielectric constant. A similar trend also can be found in the co-polarization ratio (Iodice et al., 2011). With respect to our

带格式的：字体：斜体
带格式的：字体：斜体
带格式的：字体：斜体
带格式的：字体：斜体
带格式的：字体：斜体
带格式的：字体：斜体
带格式的：字体：斜体
带格式的：字体：斜体
带格式的：字体：斜体

simulated results shown in Figs.1 and 2, it is important to note that the proposed parameter *CP-Ratio* is sensitive to the variation of the dielectric constant and almost insensitive to surface slope variations if $\sigma < 0.15$.

For our analysis we use the fact that a dry snow layer is transparent at C and L frequencies (meaning that our method is only applicable under freezing conditions), and we do not consider metamorphosis of the basal snow layer due to brine wicking effects or due to melt-freeze cycles. We focus on undeformed Arctic young and first-year ice for which volume scattering is low because of the relatively high ice salinity, which means that the ice surface is the dominant scattering source. Then the backscattering coefficients depends on the small-scale surface roughness and the dielectric constant of the ice surface. Desalination of the ice occurs parallel to its growth due to brine drainage (Kovacs, 1996). The desalination process causes a decrease of the dielectric constant. Hence the basic idea of our method for retrieving ice thickness is to relate changes of the dielectric constant to ice thickness growth. Because the *CP-Ratio* is sensitive to the variation of the dielectric constant, it is well-suited for detecting changes of the ice thickness of smooth first-year level ice.

带格式的：字体：斜体

带格式的：字体：斜体

3 A simulation study

3.1 Forward scattering model

In this section, we describe the combined use of an ice growth model and an electromagnetic scattering model for level sea ice to study sensitivities of *CP-Ratio* to different ice and radar properties. We applied the scattering model proposed by (Nghiem et al., 1995) to simulate the sea ice volume scattering and absorption by brine inclusions. The surface contribution was calculated with the polarimetric two-scale model (PTSM) (Iodice et al., 2011, 2013) and incoherently added to the volume term.

The sea ice scattering model configuration is presented in Fig. 3. Note that we do not explicitly include a snow layer (see also section 2.3). The effects of a dry snow layer

are (1) the dielectric contrast between ice and snow is lower than between ice and air, hence the reflectivity of the ice surface is lower; (2) the radar wavelength in the snow is shorter than in air, hence the ice surface appears rougher to the radar; (3) the incidence angle gets steeper (depending on the dielectric constant of the snow), which (relatively) causes a stronger backscattering. Since we carry out simulations with different dielectric constants (by varying temperature and brine volume fraction), surface roughness parameters, and radar incidence angles, the results obtained without snow can be transferred to cases with dry snow layers.

In our model, the uppermost layer is air with permittivity ε_0, the lowermost medium is seawater with complex permittivity ε_2, both enclosing the ice layer. The sea ice background is assumed to be pure ice with complex permittivity ε_i. The complex permittivity of brine inclusions is ε_b, and their fractional volume is f_v. The relative permittivity of the sea ice ε_{eff} is a function of the volume fraction of brine inclusions (Arcone et al., 1986; Vant et al., 1978). The ice surface roughness is described by the correlation length l, rms height s, and the standard deviation of surface slope σ. The thickness and surface temperature of the sea ice layer are H and T_0, respectively. Lastly, the magnetic permeability of free space is μ_0. Thickness and permittivity of sea ice are subject to dynamic changes during the ice growth process. The small-scale surface roughness (on cm-scale) may also vary temporally and spatially. This, however, can hardly be measured in the field with sufficient spatial density over larger areas. Here we do neither consider deformation processes causing surface roughness components on the order of meters. Furthermore, we assume that the scattering contribution of the ice-water interface can be neglected because of the relatively high salinity of Arctic young and first-year ice. Very thin ice for which reflections of the radar waves between surface and bottom have to be considered is excluded from this study. In our simulations, we do not take a snow cover into account. We restrict our analysis to temperatures well below freezing point, which means that a dry snow layer would change the incidence angle and the dielectric contrast at the ice surface. In case of the ice growth simulations described below, the snow has an insulating effect that changes the rate of ice thickness growth. Hence, various scenarios can be constructed,

which is beyond the scope of this paper, which we regard as a first step towards developing a methodology for ice thickness retrieval using CP SAR.

For ice growth simulations we use a 1-D thermodynamic model developed by Maykut, (1978, 1982) based on the energy balance equations at the atmosphere-ocean boundary. The balance of the heat fluxes at the upper surface of the ice can be expressed as:

$$(1-\alpha)F_r - I_0 + F_L - F_E + F_S + F_e + F_C = 0. \quad (13)$$

where F_r is the incident short wave radiation, αF_r is the short wave radiation reflected by ice, and α is the albedo. I_0 is the amount of shortwave radiation absorbed in the interior of the ice layer, F_L is the incoming long wave radiation, F_E is the long wave radiation emitted by the ice, F_S is the sensible heat flux, and F_e is the latent heat flux. The last term F_C is the upward conductive heat flux that is the heat from the bottom interface conducted through the ice to the upper surface. We assume that the temperature at the ice-water interface is at -1.8°C. The equations and parameters used in this study are listed in Table 1.

Substituting the equations and parameters listed in Table 1 into the Eq. (13) and using the Newton-Raphson iteration method, the sea ice surface temperature T_0 is obtained. Once T_0 is known, F_E, F_S, F_e and F_C can be easily calculated. A linear temperature profile within the sea ice layer is assumed. For volume scattering and absorption calculations we use a mean ice temperature (T) calculated from the melting temperature at the ice-water interface temperature (T_b = -1.8 °C) and the ice surface temperature (T_0). Furthermore, the thickness H (cm), density ρ (kg m^{-3}), brine volume fraction f_{vb}, and permittivity ε_{eff} of sea ice, which are directly related to the volume scattering and absorption in the ice, are obtained by the equations given in Table 2. The ice surface roughness parameters s, l and σ are set to different values considering the validity range of the X-SPM model (Ulaby et al., 1982; del Monaco et al., 2009; Iodice et al., 2011).

3.2 Simulation results

To assess theoretical possibilities and limitations of ice-thickness measurements by *CP-Ratio*, we simulated the evolution of ice growth for given temperature and wind conditions based on the growth model described in Sect. 3.1. The air temperature and wind speed were set to -12°C and 10.5 m s^{-1}, respectively, throughout this simulation, based on reports from the field measurements that are described in section 4 below. The simulation started at an initial ice thickness of 1.0 cm. A finite difference scheme was used to calculate the increase of ice thickness at every 1 h step. After executing about 25 days' simulation, the following parameters were extracted as a function of time to drive the sea ice scattering model: ice permittivity ε_{eff}, thickness of ice layer H, and volume fraction of brine inclusions f_{vb}. For evaluating the rough surface scattering contribution, we took roughness data reported in Onstott (1992, Table 5-3) who listed them for different stages of ice growth: (1) s=0.031 cm and l=1.26 cm (ks = 0.035, kl = 1.4 for the radar frequency of 5.4 GHz, k - wavenumber) for dark nilas, (2) s=0.12 cm and l=1.45 cm (ks = 0.14, kl = 1.6) for light nilas, and (3) s=0.11 cm and l=0.54 cm (ks = 0.12 and kl = 0.6) for smooth first-year ice. We note that we will use these roughness values for first-year ice in general, considering the large variability of small-scale ice surface roughness. The values are in the validity range of the original Bragg scattering theory and should hence be fully covered by the X-SPM model presented in Iodice et al. (2011). The standard deviation of the large-scale slope σ is ranging according to the validity range of the X-SPM model (Iodice et al., 2011).

At this point we note that a systematic relationship between small-scale surface roughness and ice thickness has never been reported. Weathering effects, melt events, and snow metamorphism influence the millimeter-to-centimeter ice surface roughness to a highly variable extent, independent of ice thickness. As we will show below, the influence of the small scale roughness on *CP-Ratio* is moderate to low, hence the issue of varying small-scale surface roughness is not very critical.

Figure 4 illustrates the simulated sea ice thickness as a function of time, and ice temperature, and volume fraction of brine inclusions as functions of ice thickness.

删除的内容: examples from

删除的内容: esen

删除的内容: which are given

删除的内容: dark nilas (thickness 5 cm) with

删除的内容:),

删除的内容: light nilas (10 cm) with

删除的内容:),

删除的内容: smooth first-year ice (>2 m) with

删除的内容:). These

删除的内容: from 0.05 up to 0.4

Figure 4 clearly shows that the volume fraction of of brine inclusions reduces due to desalination processes as the ice thickness increases.

To investigate the dependence of *CP-Ratio* on the radar incidence angle and ice thickness, the complex scattering coefficients (S_{HH}, S_{VV}, and S_{HV}) were computed for C-band (5.4 GHz) at incidence angles of 20° - 60°. Then the *CP-Ratio* was calculated from Eq. (12). The relationship between *CP-Ratio* and sea ice thickness at case (3) (first year ice roughness conditions given above) and σ = 0.1 is shown in Fig. 5. It reveals that *CP-Ratio* exhibits a monotonically decreasing trend with growing ice-thickness at constant incidence angles. It should be noted that the sensitivity of *CP-Ratio* to vertical ice growth is much higher at smaller ice-thickness values up to approximately 0.4 m. This can be explained by fact that the ice salinity is calculated according to the relationship proposed by (Cox and Weeks, 1983). Their parameterization of salinity as a function of ice thickness reveals a discontinuity at a thickness of 0.4 m.

Figure. 6 and 7 indicate the roughness dependencies of the *CP-Ratio*. In Fig. 6 the standard deviation of surface slope σ is varied from 0.05 to 0.4 and the small-scale roughness is fixed at the case 2 roughness condition (s=0.12 cm, l=1.45 cm). When σ is smaller, the effect of the variability of the ice-surface slope on the sensitivity of the *CP-Ratio* to ice thickness is small; however, at larger values of σ this effect becomes significant and weakens the capability of *CP-Ratio* to estimate thickness. Given the same σ-values, the magnitude of *CP-Ratio* is higher at larger than at smaller incidence angles, while the sensitivity (given by the local slope of the curves) does hardly change, as depicted in Figure 7, where we show examples for case 2 (moderate) ice roughness. The sensitivity as a function of ice thickness remains basically the same for all incidence angles. A larger magnitude of *CP-Ratio* means that it is less affected by noise (see equation 11). From the results of these simulations, we expect that the proposed new parameter for thickness retrieval has a strong correlation with the thickness of smooth undeformed sea ice over all incidence angles, and the sensitivity is larger for thinner (<0.4 m) than for thicker sea ice. At larger incidence angles, the reduction of the radar wavelength in a snow layer on top of the ice is not a critical

删除的内容: as ice thickness increases

带格式的: 字体颜色: 自动

带格式的: 字体:斜体

删除的内容: (light nilas)

删除的内容: .

删除的内容: sensitivity

带格式的: 字体:斜体

删除的内容: .

删除的内容: reveals that the small-scale

删除的内容: has an effect on the magnitude of the *CP-Ratio* but its

删除的内容: to

删除的内容: on acceptable levels at higher

删除的内容: At

删除的内容: angles, the

删除的内容: greater than at smaller ones.

删除的内容: in particular at larger

issue, since the effect of the small-scale roughness on *CP-Ratio* is low in this case. However, the snow layer also changes the incidence angle of the radar beam on the ice surface, which can have a considerable impact on the thickness retrieval in particular at thickness values larger than 0.3 to 0.4 m where the slope of the curves theoretically decreases to a low value (Fig. 7). In practice, this limitation is less critical as we show below. On first-year sea ice the bottom part of the snow layer can be saline due to brine wicking, possibly creating a dielectric interface within the snow, or resulting in brine volumes large enough to influence the radar backscatter (Barber and Nghiem, 1999; Galley et al., 2009). This may also affect the accuracy of the thickness retrieval using *CP-Ratio*. Finally, we note that the model simulations include interactions between the ice surface and the ice-water interface, which result in oscillations of the CPR for an ice thickness < 0.16 m. In the field measurements discussed below, this effect was not observed. We assume that the actual ice thickness is rarely exactly constant over larger areas.

删除的内容: n

删除的内容: has decreased

删除的内容: This regime, however, will not be taken for practical thickness retrievals

4 Datasets and experimental results

4.1 Field Study

On 19-20 March 2011, a field program was conducted by the Department of Fisheries and Oceans Canada (DFO) along the mid-Labrador coast (Fig. 8) (Prinsenberg et al., 2012a). As part of the field survey, snow thickness and ice thickness were measured with a helicopter-borne sensor package which consists of a laser altimeter, an electromagnetic induction sounder (EMS), and a ground-penetrating radar (GPR). The laser altimeter provides the distance to the snow or ice surface, whereas the induction sounder measures the distance from the sensor to the ice-water interface. Hence the snow-plus-ice thickness can be obtained (Prinsenberg et al., 2012a; 2012b). Comparisons with drill hole data showed that the ice thickness values derived from such soundings agree well within ±0.1 m over flat homogeneous ice (Haas et al., 2006; Prinsenberg et al., 2012b). The accuracy decreases over ridges and deformed ice,

where the maximum thickness can be underestimated by as much as 50 % (Haas et al., 2006; Prinsenberg et al., 2012b). Snow thickness profiles were collected concurrently with a ground-penetrating radar (GPR) and the laser altimeter measurements. The ground-penetrating radar which was operated at a frequency of 1 GHz, receives returns from the ice-snow and air-snow interfaces, though the return from air-snow surface is very weak. The laser altimetry is superior for defining the air-snow interface. Therefore, the combination of GPR and laser altimetry allows to retrieve the snow depth on sea ice. For a 1 GHz GPR system, the minimum detectable snow layer thickness is 0.12 m and the measurement error is 0.08 m in light dry snow. (Lalumiere, 2006) By subtracting the GPR snow thickness measurements from the EMS snow plus ice thickness measurements, sea ice thickness can be estimated.

删除的内容: G Hz

4.2 Data sets and data processing

All data are available on the Website of DFO including pictures, notes and reports of the survey (http://www.bio.gc.ca/science/research-recherche/ocean/ice-glace/data-donnees-eng.php).

During the field survey, four C-band RADARSAT-2 quad-polarization images were acquired nearly coincident with the DFO airborne survey flight lines (Fig. 8). The RADARSAT-2 data were provided by the MacDonald, Dettwiler and Associates Ltd (MDA). Important SAR parameters are listed in Table 3. For our processing we used the RADARSAT-2 single-look slant range complex format as starting point. A speckle reduction filter (13×13 Lee filter) and radiometric calibration procedures were applied for the calculation of the scattering matrix. With the quad-polarization data, the CTLR compact polarimetry mode can be generated via Eq. (3). Subsequently the *CP-Ratio* was extracted by Eq. (11). Lastly, the geometric registration of the simulated CP SAR images (i.e. their representation in geographical coordinates) was performed based on longitude and latitude data provided in SAR metadata.

带格式的: 字体: 斜体

Fig. 8 presents the ice condition at the study site, flight paths and four nearly coincident RADARSAT-2 fine quad-polarization images. Eight EMS profiles were measured within the coverage of the four SAR images, and the time differences

between the SAR acquisitions and EMS flights are summarized in Table 4. The images in Fig. 8 show the RADARSAT-2 data overlain with the EMS flight tracks over the fast ice and drifting pack ice. According to the ice charts, the total ice concentrations in fast-ice and pack ice regions are 10/10 and 9/10, respectively. The main ice type in land-fast is first-year ice of 70-120 cm in thickness, and the drift ice region contains grey ice (10-15 cm thick), grey-white ice (15-30 cm), thin first-year ice (30-70 cm) and again first-year ice 70-120 cm thick. In the drifting ice region several openings can be seen in the SAR images. The extent of land-fast ice evolves in the offshore direction and can be visually separated from the pack ice. Most of the rougher land-fast ice is brighter in the SAR images than the thinner undeformed land-fast ice. According to the meteorological data archive from Makkovik station (http://climate.weather.gc.ca/), the air temperature was around -9~-17 °C on 15-16 March 2011, and snow fall was registered during 2 days in the period 17-19 March with average air temperature around -15 °C. So a large fraction of the sea ice was covered with snow, which can be clearly seen in aerial photos (not shown). On 19-20 March 2011, the average air temperature was around -8~-12°C and the wind speed around 11~15 ms^{-1} (Prinsenberg et al., 2012a). Hence the snow can be regarded as dry. We also note that thermodynamically driven effects on the bottom snow layer such as brine wicking take place at temperatures higher than -7°C (Barber and Nghiem, 1999) which means that we can ignore them here for the freshly fallen snow. However, we do not have any information about elder snow layers changed by metamorphosis processes, which may have an influence on the effective backscattering signature. Nor can we exclude that sea ice flooding took place in some smaller areas. Fig. 9 shows the ice thickness and snow depth profiles of the land-fast and drift ice, indicating that the ice freeboard was mostly above the water level. The histograms shown in Fig. 9 confirm that the land-fast mean ice thickness is smaller than the one of the drifting pack ice. The percentages of areas with snow thickness above 0.2 m for land-fast and drift ice are 26.4% and 18.2% respectively. The flight profiles also show that there are deformed ice or ridges (ice thickness exceeded 2.0 m) in the survey field.

A direct comparison between SAR imagery and flight profiles data may cause errors

删除的内容: ice thickness data collected

删除的内容: open water and scattered frazil ice areas

删除的内容: heavy

删除的内容: on

删除的内容: .

删除的内容: m s

删除的内容: Fig.

删除的内容: .

删除的内容: ,

删除的内容: it, consists of rafted floes

删除的内容: reveals a deeper snow cover

带格式的: 字体颜色：深红

due to the time differences of the data acquisitions (the time difference between SAR and flight data is shown in Table 4). In addition, spatial differences may be caused by the different sampling and spatial resolutions of the measurement instruments. The sampling rate for EMS and laser is 10 Hz, which, given a typical helicopter survey speed of 80 mph, corresponds to a spatial sampling interval of about 3-4 m. While the footprint size of the laser is very small (several centimeters), the footprint of the EMS is around 20 m at a typical operation height of 5-6 m. For this experiment, the GPR was configured to a scan rate of approximately 30 scans per second. When flying at 60-80 knots, the ground sample spacing is approximately one sample per 1.0-1.5 m. Moreover, according to the DFO survey report, the floating ice drifted 1.4-1.8 knots towards southeast, as measured by ice beacons (Prinsenberg et al., 2012a). In order to mitigate the errors caused by time and spatial resolution differences, we developed the following processing chain for linking SAR and airborne data.

1. The correction of the time difference was only implemented for the drifting ice region. The boundary between fast ice and drifting pack ice was taken from ice charts of the Canadian Ice Service (Fig. 8). For the eight EMS profiles, P1, P2, P5, and P7 are in or near the land-fast ice region, whereas P3, P4, P6, and P8 are from the drift ice zone. With an ice drift speed of 1.5 knots, and drift direction southeast taken from the DFO survey report and considering the respective time differences, the profiles P3, P4, P6, and P8 are shifted to their approximate positions at the acquisition time of the SAR images. The shifted profiles are presented in Fig. 8 (dotted line). It should be noted that 28 hours passed between the acquisition times of the P8 and SAR data, and the corrected location of P8 is beyond the coverage of the SAR image. Hence P8 was discarded from further analysis.

2. The EMS (ice plus snow) thickness values below 0.1 cm were removed to consider the measurement accuracy of the EMS. Regions for which only EMS data but no GPR data are available were also removed.

3. Regions with GPR snow thickness values higher than 0.20 m were removed, because snow layers thinner than 0.20 m are nearly transparent to C-band radar waves, and the backscatter from the snow surface and volume can be neglected (Hall et al.,

删除的内容: a

删除的内容: different

删除的内容: the locations that should have been valid

删除的内容: new locations

2006).

4. By combining the field survey data (ice charts and aerial photos), a visual interpretation of RADARSAT-2 SAR was made, and regions of open water, land, and deformed ice were masked in the SAR images. Land was identified using the coastal line, open water areas were interpreted via backscattering and texture. Deformed ice was brighter than level ice in single-polarization SAR images, and revealed a higher entropy, which was extracted using H/A/α decomposition (Scheuchl et al., 2002). We emphasize that in step 1 most open water areas are already excluded from further analysis.

5. For ice zones of 50 m in length, averages of different parameters were evaluated. Firstly, we used the H/A/α unsupervised Wishart classifier to segment the SAR images, and each patch was regarded a homogeneous ice area with respect to its radar signature. Then the snow thickness, snow-plus-ice thickness profiles were cut into 50 m long flight track segments. The *CP-Ratio* values were evaluated from the co-located, drift-corrected, segmented SAR images, provided that the 50 m segment contained a homogeneous piece of ice. The segment length of 50 m was chosen according to the spatial resolution of the SAR image. Range and azimuth spacing of a RADARSAT-2 fine quad-polarization product are 4.7 m × 4.9 m respectively. Since we applied a 13 × 13 window for speckle reduction (see above), the effective spatial resolution is about 50 m. For the averages along transects, 13 SAR pixels, 15 EMS samples and 45 GPR samples were used.

6. The sea ice thickness was extracted from the averaged GPR snow depth and EMS snow-plus-ice thickness values.

7. Finally we calculated the *CP-Ratio* from equation (11) using the averaged complex backscattering coefficients.

This processing chain ensures that only level ice is considered for which the EMS system delivers reliable thickness data with an acceptable accuracy. The total length of the profile segments that we used in this study amounts to about 16 km (320 samples). Compared with the original data, almost 60% of the data were discarded in this processing chain (step 1: 17%, step 2: 10%, step 3: 23%, step 4: 10%).

删除的内容: , surface roughness, and simulated CP SAR data

删除的内容: averaged over

删除的内容: of 50 m in length. Considering

删除的内容: range

删除的内容: ,

删除的内容: pixel

删除的内容: the H/A/α unsupervised classification

删除的内容: Sea

4.3 Ice thickness retrieval

To investigate the possibility of using the proposed polarimetric parameter *CP-Ratio* to estimate sea ice thickness from SAR images, we plotted ice thickness values obtained during the field campaign describe against the corresponding values of *CP-Ratio* derived from the RADARSAT-2 images in Figure 10 (using all 320 samples). It can be seen that at C-band, the *CP-Ratio* shows a negative trend relative to the ice thickness as the simulated results given in Sect. 3.2 predicted. Fig. 10 reveals that the highest sensitivity occurs between 0 and 0.5 m and saturates with thickness values exceeding 1.5 m. As shown in Figs. 5 to 7, the sensitivity should be smaller for ice thickness exceeding 0.4 m. However, the slope change of the curves at 0.4 m is not as abrupt as in the theoretical curves predicted in Sect. 3.2. This can be presumably explained by the fact that we average over segments with different values of ice roughness parameters s, l and σ. We also need to consider that the salinity-thickness parameterization proposed by Cox and Weeks (1983) includes a discontinuity in the slope of the salinity curve at a thickness of 0.4 m, which may not exist in reality.

Since our data comprise different incidence angles (29°, 42° and 49° at the survey positions, Table 3), we can construct the relationships between ice-thickness and the *CP-Ratio* dependent on the incidence angle. We applied two different fits, a linear and a logarithmic one, to obtain an empirical relationship between the ice thickness and *CP-Ratio*. The best regression was obtained using a logarithmic function (Fig. 10). For Fig. 10, the empirical equations and correlation coefficients (CC) are

$$\begin{cases} \text{CP - Ratio} = 0.04935 - 0.07329\ln(H) & \text{for } 29^{o} \text{ incident angle } (\text{CC} = 0.90) \\ \text{CP - Ratio} = 0.06345 - 0.08251\ln(H) & \text{for } 42^{o} \text{ incident angle } (\text{CC} = 0.93) \\ \text{CP - Ratio} = 0.07744 - 0.07952\ln(H) & \text{for } 49^{o} \text{ incident angle } (\text{CC} = 0.89) \end{cases} \quad (14)$$

where all data points (320 samples) are used to derive the empirical regressions in the thickness range from 0.1–1.8 m. The reason to include larger ice thickness values is

带格式的: 字体:斜体

删除的内容: described above

删除的内容: (

带格式的: 字体:斜体

删除的内容: are plotted in Fig. 10

带格式的: 字体:斜体

删除的内容: since

带格式的: 字体:斜体

带格式的: 字体:斜体

that they can be measured with a larger accuracy, hence leading to a more robust relationship at least for the moderate thickness values between 0.4 and 0.8 m. However, to our knowledge the distribution of *CP-Ratio* due to speckle has not been derived yet which makes it difficult to judge its variation. The smallest values of *CP-Ratio* observed are about 0.03, which may indicate the noise level of *CP-Ratio*. The measured values of *CP-Ratio* for ice thickness values > 0.2 m shown in Fig. 10 are lower than the theoretical computations. This can presumably be explained by the fact that underlying theoretical models are an over-simplification of the actual situation. We note that due to the limitation of sample points, the fit for 49° incident angle is mainly determined by ice thickness values > 0.5 m.

We found that the level of the *CP-Ratio* increases as the incidence angle increases at a given value of the sea ice thickness. This observation compares well with the forward simulation studies as shown in Fig. 5. These high correlations enable us to derive reliable thickness information for smooth level ice from radar images assuming winter conditions (dry snow, no brine wicking). The ice thickness can be estimated using an exponential function, which can be described as follows:

$$H = \exp\left[\frac{a - (\text{CP - Ratio})}{b}\right]. \quad (15)$$

where a and b are the coefficients of the exponential fit.

At the next stage, we focused on the RADARSAT-2 images #2 and #3 (which have the same incidence angle of 42°) to validate our method. Out of total 320 samples, 159 samples belong to images #2 and #3. According to the principle of independent sample test, we divided these 159 samples into two data sets in an arbitrary way. The first set includes 79 samples that are used to fit the model for estimating ice thickness and the second one comprises 80 samples that serve to retrieve ice thickness and compare the results with the data from the field campaign. The coefficients a and b of the empirical fit generated from the first data set are 0.068 and 0.077 respectively. Note that these coefficients are different from those derived in Eq. (14) from the same two SAR images, because now less points could be used to derive the fit. The fitted curve and validation results are presented in Fig. 11a and Fig. 11 b, respectively. The

带格式的：字体：斜体

删除的内容：.

correlation coefficient for the fit shown in Fig 11a is 0.93 for the thickness range from 0.1 to 1.8 m and 0.94 for the thickness range from 0.1 to 0.8. The RMS error and the relative error between the observed and the estimated ice thickness, shown in Fig. 11b, are 12 cm and 20% in the thickness range from 0.1–1.8 m, and 8 cm and 17% for 0.1 to 0.8 m. The relative RMS error implies, e.g. that the absolute RMS error is 0.2 m at an ice thickness of 1.0 m (for the range 0.1 to 1.8 m). Figure 11b also demonstrates that the error of the retrieved ice thickness is very large at values > 0.8 m which is to be expected from the theoretical curves, considering the significantly decreased sensitivity of *CP-Ratio* to larger ice thickness.

删除的内容: 6

删除的内容: 18% for 0.1 to 0.6 m (the latter case considers the decreased sensitivity of *CP-Ratio* to larger ice thickness as discussed above).

带格式的: 字体:Times New Roman

5 Discussion and conclusion

This paper provides a first analysis of sea ice thickness retrieval using compact polarimetric SAR. We developed a new parameter that we call *CP-Ratio* to estimate the thickness of undeformed first-year level ice from C-band radar images, under dry snow conditions (snow depth < 20 cm). Numerical model simulations showed that this parameter is sensitive to changes of the dielectric constant that are linked to the growth of sea ice. We developed empirical relationships for the retrieval of level ice thickness from *CP-Ratios*. For the validation of our results we also employed RADARSAT-2 images for which thickness values were available. The optimal regression between *CP-Ratio* and ice thickness was achieved with an exponential fit. The RMS error was 12 cm, and the relative error amounted to 20% for a thickness range between 0.1 and 1.8 m, and 8 cm and 17% for the range between 0.1 and 0.8 m. This indicates that the proposed parameter is very useful for the retrieval of first-year level ice thickness between 0.1 and 0.8 m.

Since the thickness of deformed ice can be underestimated by the EMS measurements by as much as 50 or 60 % in the worst cases, we could only study the case of level ice. The capability of CP SAR to retrieve the thickness of deformed ice, which reveals a larger variation of large-scale roughness with respect to the sensor resolution, needs to be further discussed and studied.

带格式的: 字体:斜体

带格式的: 字体:斜体

删除的内容: 18

删除的内容: 6

删除的内容: , even in the thickness range

删除的内容: > 1

删除的内容: is

Although our tests are performed on a limited sample of images, our findings demonstrate that the C-band compact polarimetric SAR has a potential for sea-ice thickness retrievals over level first-year ice covered by a thin dry snowpack. The issue of environmental factors affecting the retrieval accuracy, e. g. brine wicking in the snow, or snow layers with different dielectric properties, has to be investigated further in more detail. The several planned Earth-observing satellite missions supporting compact polarimetry (e.g. the RCM operated at C-band) will provide the wide swath coverage necessary for operational sea ice monitoring. Hence our approach potentially provides a new operational tool for sea ice thickness measurements with a large areal coverage. In this case, the resulting thickness products are also of interest for the development, improvement, and validation of forecast models for the prediction of ice conditions, or of seasonal and climate simulations that consider Arctic and Antarctic ice conditions.

Acknowledgment

This study was supported by the National Nature Science Foundation of China under Grant 41306193, and the R&D Special Foundation for Public Welfare Industry (201305025). This work was carried out as part of the Dragon-3 Programme (10501) by the Ministry of Science and Technology of the P. R. China and the European Space Agency. The authors would like to thank the Canadian Space Agency (CSA) and MDA for providing the RADARSAT-2 data, and we are very thankful to the department of Fisheries and Oceans Canada for their support in providing valuable snow and sea ice field data. We gratefully acknowledge the detailed comments of Stefan Kern and two anonymous reviewers which helped to considerably improve the readability of the article.

References

Arcone, A., Gow, A. G., and McGrew, S.: Structure and dielectric properties at 4.8 and 9.5 GHz of saline ice, J. Geophys. Res., 91, 14281–14303, 1986.

Barber, D. G., and Nghiem, S. V.: The role of snow on the thermal dependence of microwave backscatter over sea ice, J. Geophys. Res., 104, 25789-25803, 1999.

Behrendt, A., Dierking, W., Fahrbach, E., and Witte, H.: Sea ice draft in the Weddell Sea, measured by upward looking sonars, Earth Syst. Sci. Data, 5(1), 209-226, doi:10.5194/essd-5-209-2013, 2013.

Charbonneau, F. J., Brisco, B., Raney, R. K., McNairn, H., Liu, C., Vachon, P., Vachon, W., Shang, J., DeAbreu, R., Champagne, Merzouki, A., and Geldsetzer, T.: Compact polarimetry overview and applications assessment, Can. J. Remote Sens., 36, 298–315, 2010.

Cox, G. and Weeks, W.: Equations for determining the gas and brine volumes in sea-ice samples, J. Glaciol., 29, 306–316, 1983.

Cox, G. and Weeks, W.: Numerical simulations of the profile properties of undeformed first-year sea ice during the growth season, J. Geophys. Res., 93, 12449–12460, 1988.

Dabboor, M. and Geldsetzer, T.: Towards sea ice classification using simulated RADARSAT Constellation Mission compact polarimetric SAR imagery, Remote Sens. Environ., 140, 189–195, 2014.

del Monaco, F. D., Quattro, N. D., Iodic, A., and Natale, A.: Extended small perturbation method and retrieval of natural surface parameters, in: Proc. 6th Eur. Radar Conf., Rome, Italy, 537–540, 2009.

Dierking, W.: Laser profiling of the ice surface topography during the Winter Weddell Gyre Study 1992, J. Geophys. Res., 100, 4807–4820, 1995.

Dierking, W.: Sea ice monitoring by synthetic aperture radar, Oceanography, 26, 100–111, doi: 10.5670/oceanog.2013.33, 2013.

Fukusako, S.: Thermophysical properties of ice, snow, and sea ice, Int. J. Thermophys., 11, 353–372, 1990.

Fung, A. K. and Eom, H. J.: Application of a combined rough surface and volume scattering theory to sea ice and snow backscatter, IEEE T. Geosci. Remote Sens., GE-20, 528–536, 1982.

Fung, A. K.: Microwave Scattering and Emission Models and Their Applications.

Artech House, Boston, London, 1994.

Galley, R. J., Trachtenberg, M., Langlois, A., Barber, D. G., and Shafai, L.: Observations of geophysical and dielectric properties and ground penetrating radar signatures for discrimination of snow, sea ice and freshwater ice thickness. Cold Reg. Scie. Technol., 57, 29-38. 2009.

Geldsetzer, T., Arkett, M., Zagon, T., Charbonneau, F., Yackel, J. J., and Scharien, R.: All season compact-polarimetry SAR observations of sea ice, Canadian J. of Remote Sens., doi: 10.1080/07038992.2015.1120661, 2015.

Goebell, S.: Comparison of coincident snow-freeboard and sea ice thickness profiles derived from helicopter-borne laser altimetry and electromagnetic induction sounding, J. Geophys. Res., 116, C08018, doi:10.1029/2009JC006055, 2011.

Haapala, J., Lensu, M., Dumont, M., Renner, A. H. H., Granskog, M. A., and Gerland, S.: Small-scale horizontal variability of snow, sea-ice thickness and freeboard in the first-year ice region north of Svalbard, Ann. Glaciol., 54, doi: 10.3189/2013AoG62A157, 2013.

Haas, C., Gerland, S., Eicken, H., and Miller, H.: Comparison of sea-ice thickness measurements under summer and winter conditions in the Arctic using a small electromagnetic induction device, Geophysics, 62, 749–757, 1997.

Haas, C., Hendricks, S., and Doble, M.: Comparison of the sea ice thickness distribution in the Lincoln Sea and adjacent Arctic Ocean in 2004 and 2005, Ann. Glaciol., 44, 247–252, 2006.

Hajnsek, I., Pottier, E., and Cloude, S. R.: Inversion of surface parameters from polarimetric SAR, IEEE T. Geosci. Remote Sens., 41, 727–744, 2003.

Hall, D. K., Kelly, R. E., Foster, J. L., and Chang, A. T.: Estimation of Snow Extent and Snow Properties. Encyclopedia of Hydrological Sciences, 5-55, 2006.

Hendricks, S., Gerland, S., Smedsrud, L.H., Hass, C., Pfaffhuber, A., and Nilsen, F.: Sea-ice thickness variability in Storfjorden, Svalbard, Ann. Glaciol., 52, 61-68, 2011.

Huntemann, M., Heygster, G., Kaleschke, L., Krumpen, T., Mäkynen, M., and Drusch, M.: Empirical sea ice thickness retrieval during the freeze-up period from SMOS

high incident angle observations, The Cryosphere, 8, 439–451, doi:10.5194/tc-8-439-2014, 2014.

Iodice, A., Natale, A., and Riccio, D.: Polarimetric two-scale model for soil moisture retrieval via dual-Pol HH-VV SAR data, IEEE J. Sel. Top. Appl., 6, 1163–1171, 2013.

Iodice, A., Natale, A., and Riccio, D.: Retrieval of soil surface parameters via a polarimetric two-scale model, IEEE T. Geosci. Remote Sens., 49, 2531–2547, 2011.

Ji, S. Y., Yue, Q. J., and Zhang, X.: Thermodynamic analysis during sea ice growth in the Liaodong Bay, Mar. Environ. Sci., 19, 35–39, 2000.

Kim, J. W., Kim, D. J., and Hwang, B. J.: Characterization of Arctic sea ice thickness using high-resolution spaceborne polarimetric SAR data, IEEE T. Geosci. Remote Sens., 50, 13–22, 2012.

Kovacs, A., Valleau, N. C., and Holladay, J. S.: Airborne electro- magnetic sounding of sea ice thickness and sub-ice bathymetry, Cold Reg. Scie. Technol., 14, 289–311, 1987.

Kovacs, A.: Sea Ice, Part I.: Bulk Salinity versus Ice Floe Thickness, USA Cold Regions Research and Engineering Laboratory, CRREL Rep. 97, United States Army, Corps of Engineers, 1–16, 1996.

Kwok, R., and Cunningham, G. F.: ICESat over Arctic sea ice: Estimation of snow depth and ice thickness, J. Geophys. Res., 113, C08010, doi: 10.1029/2008JC004753, 2008.

Kwok, R., Cunningham, G. F., Wensnahan, M., Rigor, I., Zwally, H. J., and Yi, D.: Thinning and volume loss of the Arctic Ocean sea ice cover: 2003–2008, J. Geophys. Res., 114, C07005, doi: 10.1029/2009JC005312, 2009.

Kwok, R., Nghiem, S. V., Yueh, S. H., and Huynh, D. D.: Retrieval of thin ice thickness from multifrequency polarimetric SAR data, Remote Sens. Environ., 51, 361–374, 1995.

Kwok, R.: Satellite remote sensing of sea ice thickness and kinematics: a review, J. Glaciol., 56, 1129-1140, 2010.

已下移 [1]: Kaleschke, L.,

删除的内容: Tian-Kunze, X.,

已下移 [2]: Maaß, N., Mäkynen, M.,

删除的内容: and Drusch, M.: Sea ice thickness retrieval from SMOS brightness temperatures during the Arctic freeze-up period, Geophys. Res. Lett., 39, 1–5, doi: 10.1029/2012GL050916, 2012.

Lalumiere, L.: Ground penetrating radar of helicopter snow and ice surveys, Can. Tech. Rep. Hydrogr. Ocean Sci., 248, 1–50, http://publications.gc.ca/collections/collection_2015/mpo-dfo/Fs97-18-248-eng.pdf, 2006.

Laxon, S. W., Giles, K. A., Ridout, A. L., Wingham, D. J., Willatt, R., Cullen, R., Kwok, R., Schweiger, A., Zhang J., Haas, C., Hendricks, S., Krishfield, R., Kurtz, N., Farrell, S. and Davidson, M.: CryoSat-2 estimates of Arctic sea ice thickness and volume, Geophys. Res. Lett., 40, 732–737, doi: 10.1002/grl.50193, 2013.

Maykut, G. A.: Energy exchange over young sea ice in the central Arctic, J. Geophys. Res., 83, 3646–3658, 1978.

Maykut, G. A.: Large-scale heat exchange and ice production in the central Arctic, J. Geophys. Res., 87, 7991–7984, 1982.

Nakamura, K., Wakabayashi, H., Naoki, K., Nishio, F., Moriyama, T., and Uratsuka, S.: Observation of sea-ice thickness in the sea of Okhotsk by using dual-frequency and fully polarimetric airborne SAR (Pi-SAR) data, IEEE T. Geosci. Remote Sens., 43, 2460–2469, 2009a.

Nakamura, K., Wakabayashi, H., Uto, S., Ushio, S., and Nishio, F.: Observation of sea-ice thickness using ENVISAT data from Lützow- Holm Bay, East Antarctica, IEEE Geosci. Remote Sens. Lett., 6, 277-281, 2009b

Nghiem, S. V., Kwok, R., Yueh, S. H., and Drinkwater, M. R.: Polarimetric signatures of sea ice, theoretical model, J. Geophys. Res., 100, 13665–13679, 1995.

Nord, M. E., Ainsworth, T. L., Lee, J. S., and Stacy, N. J. S.: Comparison of compact polarimetric synthetic aperture radar modes, IEEE T. Geosci. Remote Sens., 47, 174–188, 2009.

Onstott, R.: SAR and scatterometer signatures of sea ice, in Microwave Remote Sensing of Sea Ice, Geophysical Mono. 68, Carsey, F., Ed., Washington, DC: Amer. Geophys. Union, pp. 73–104, 1992.

Prinsenberg, S. J., Peterson, I. K., Holladay, J. S., and Lalumiere, L.: Labrador shelf pack ice and iceberg survey, March 2011, Can. Tech. Rep. Hydrogr. Ocean Sci., 275, 1–44, http://www.ocean-sci.net/275/1/2012/, 2012a.

Prinsenberg, S., Hollady S., and Lee J.: Measuring ice thickness with EISflow, a fixed-mounted helicopter electromagnetic-laser system, Proc. 12th International Off-shore and Polar Engineering Conference, Kitakyushu, Japan, 737-740, 2012b.

Raney, R.: Hybrid polarity SAR architecture, IEEE T. Geosci. Remote Sens., 45, 3397–3404, 2007.

Rossiter, J. R., and Holladay, J. S.: Ice-thickness measurement, in Remote Sensing of Sea Ice and Icebergs, edited by Haykin, S. et al., pp. 141–176, John Wiley, Hoboken, N. J., 1994.

Rothrock, D. A., Yu, Y., and Maykut, G. A.: Thinning of the Arctic sea-ice cover, Geophys. Res. Lett., 26, 3469–3472, doi: 10.1029/1999GL010863, 1999.

Scheuchl, B., Flett, D., Caves, R., and Cumming, I.: Potential of RADARSAT-2 data for operational sea ice monitoring, Canadian J. of Remote Sens., 30, 448-461, 2004.

Scheuchl, B., Hajnsek, I., and Cumming, I.: Sea ice classification using multi-frequency polarimetric SAR data, in: Geosci. Remote Sens. Symposium, IGARSS'02, Toronto, Canada, 1914-1916, 2002.

Soulis, E. D., Lennox, W. C., and Sykes, J. F.: Estimation of the thickness of undeformed first year ice using radar backscatter, in: Geosci. Remote Sens. Symposium, IGARSS'89, Vancouver, Canada, 2366–2369, 1989.

Souyris, J. C., Imbo, P., Fjortoft, R., Mingot, S., and Lee, J. S.: Compact polarimetry based on symmetry properties of geophysical media: The π/4 mode, IEEE T. Geosci. Remote Sens., 43, 634–646, 2005.

Tian-Kunze, X., Kaleschke, L., Maaß, N., Mäkynen, M., Serra, N., Drusch, M., and Krumpen, T.: SMOS-derived thin sea ice thickness: algorithm baseline, product specifications and initial verification, The Cryosphere, 8, 997-1018, doi:10.5194/tc-8-997-2014, 2014.

Toyota, T., Nakamura, K., Uto, S., Ohshima, K. I., and Ebuchi, N.: Retrieval of sea ice thickness distribution in the seasonal ice zone from airborne L-band SAR, Int. J. Remote Sens., 30, 3171–3189, 2009.

Ulaby, F. T., Moore, R. K., and Fung, A. K.: Microwave Remote Sensing: Active and

已移动(插入) [1]
已移动(插入) [2]

Passive, vols. II, Addison-Wesley, Reading, MA, 1982.

Vancoppenolle, M., Fichefet, T., and Bitz, C. M.: On the sensitivity of undeformed Arctic sea ice to its vertical salinity profile, Geophys. Res. Lett., 32, L16502, doi:10.1029/2005GL023427, 2005.

Vant, M. R., Ramseier, R. O., and Makios, V.: The complex dielectric constant of sea ice at frequencies in the range 0.1 to 40 GHz, J. Appl. Phys., 49, 1264–1280, 1978.

Wadhams, P., Tucker III, W. B., Krabill, W. B., Swift, R. N., Comiso, J. C., and Davis, N. R.: Relationship between sea ice freeboard and draft in the Arctic Basin, and implications for ice thickness monitoring, J. Geophys. Res., 97, 20325–20334, doi: 10.1029/92JC02014, 1992.

Wadhams, P.: A comparison of sonar and laser profiles along corresponding tracks in the Arctic Ocean, in: Sea Ice Processes and Models, edited by: Pritchard, R. S., Univ. of Washington Press, Seattle, Wash., 283–299, 1980.

Wakabayashi, H., Matsuoka, T., and Nakamura, K.: Polarimetric characteristics of sea ice in the Sea of Okhotsk observed by airborne L-band SAR, IEEE T. Geosci. Remote Sens., 42, 2412–2425, 2004.

Wang, X., Key, J. R., and Liu, Y.: A thermodynamic model for estimating sea and lake ice thickness with optical satellite data, J. Geophys. Res., 115, C12035, doi: 10.1029/2009JC005857, 2010.

Yue, Q. J., Ji, S. Y., Miao, W. D., and Wu, S. L.: Solar radiation on sea ice in Liaodong Bay, Oceanol. ET Limnol. Sin., 31, 562–567, 2000.

删除的内容:

带格式的: 字体:Times New Roman

带格式的: 缩进: 左: 0 cm, 悬挂缩进: 1 字符, 首行缩进: -1 字符

Table 1. Equations and parameters used for the sea ice thermodynamic model

Term	Equations	Parameters	Comments
The incident short wave radiation	$F_r=(1–0.0065C^2)Q_{so}a^m$ (Ji et al., 2000; Yue et al., 2000)	$a^m=0.99–0.17m$	a^m is the atmospheric transmissivity; C is the cloud coverage; Q_{so} is the solar irradiance for the D^{th} day in a year; I_s is the solar radiation constant (unit: W/m^2); δ is the declination angle of
		$m=0.83$	
		C in the range 0~1	
	$Q_{so}=Q_s$ ($\sin\beta \sin\delta + \cos\beta \cos\delta \cos H_a$)	$Q_s=I_s(1+0.033\cos(2\pi D/365))$	

	(Yue et al., 2000)	δ=23.44°cos[(172–D)2π/365] H_a=15(t-12)π/180+λ	the sun; H_a is the local solar hour angle; β and λ are the latitude and longitude; t is Coordinated Universal Time.
The long wave radiation	$F_E = \varepsilon_i \sigma T_0^4$ (Maykut, 1978)	σ=5.670×10^{-8} ε_i=0.97	σ is the Stefan-Boltzman constant (unit: w/(m^{2}K^4)); T_0 is the surface temperature of sea ice (unit: K); T_a is the air temperature (unit: K); ε_i is the emissivity of sea ice; ε_a is the emissivity of atmosphere; e is the water vapor pressure at T_a (unit: HPa).
	$F_L = (1+kC^2)\varepsilon_a \sigma T_a^4$ (Maykut, 1978)	k=0.0017 ε_a=0.55+e×0.052$^{1/2}$	
The sensible heat flux	F_s=$\rho_a C_p C_s u(T_a$-$T_0)$ (Cox and Weeks, 1988)	ρ_a=1.3 C_p=1006 C_s=0.003	ρ_a is the air density (unit: kg/m^3); C_p is the specific heat at constant pressure (unit: J/(kg·K)); C_s is the sensible heat transfer coefficient; u is the wind speed;
The latent heat flux	F_e=$\rho_a L C_e u(q_a$-$q_0)$ (Cox and Weeks, 1988)	C_e=0.00175 L=2.5×10^6–2.274×10^3(T_a–273.15)	L is the latent heat of vaporization (unit: J/kg);
	$q_a - q_0 = \frac{0.622}{p_0} \cdot \begin{bmatrix} a(fT_a^4 - T_0^4) + b(fT_a^3 - T_0^3) + \\ c(fT_a^2 - T_0^2) + d(fT_a - T_0) + \\ e(f-1) \end{bmatrix}$ (Cox and Weeks, 1988)	p_0=1013 a=2.7798202×10^{-6} b=-2.6913393×10^{-3} c=0.97920849; d=-158.63779 e=9653.1925;	p_0 is the surface atmospheric pressure (unit: mbar); f is the relative humidity; a, b, c, d, and e are constants; a (unit: k^4), b (unit: k^3), c (unit: k^2), d (unit: k)
The albedo of sea ice	$\alpha = \beta_0 + \beta_1 H + \beta_2 H^2 + \beta_3 H^3$ (Cox and Weeks, 1988)	β_0=0.2386; β_1=6.015×10^{-3} β_2=-4.882×10^{-5}; β_3=1.267×10^{-7}	H is the sea ice thickness (unit: cm).
The absorbed shortwave radiation	I_0=$i_0(1-\alpha)F_r$ (Maykut, 1978; Cox and Weeks, 1988)	i_0=17%	i_0 is the percent.

删除的内容:

The upward conductive heat flux	$F_C = (k/H)(T_b - T_0)$ (Cox and Weeks, 1988)	$k = k_i(1-f_{vb}) + k_b f_{vb}$ $k_i = 4.17\times10^4[5.35\times10^{-3} - 2.568\times10^{-5}(T_0 - 273.15)]$ $k_b = 4.17\times10^4[1.25\times10^{-3} + 3.0\times10^{-5}(T_0 - 273.15) + 1.4\times10^{-7}(T_0 - 273.15)^2]$ T_b=-1.8	k, k_i, k_b are the conductivity of ice layer, pure ice and pure brine, respectively (unit: W/m/K); T_b is the freezing point at 35 salinity (unit: °C); f_{vb} is volume fraction of sea ice brine inclusion.

Table 2. Equations and parameters used for the sea ice properties

Term	Equations	Parameters	Comments
The ice thickness	$\frac{\Delta h}{\Delta t} = \frac{F_C(H)}{\rho L_f}$ (Cox and Weeks, 1988) $H = \sum_{i=0}^{Time} \frac{\Delta h}{\Delta t} \Delta Time$	L_f=4.187×10^3(79.68–0.505T_b–0.0273S_i)+4.3115S_i/T_b+8×10^{-4} T_b S_i–0.009(T_b)^2 (Fukusako,1990)	$\frac{\Delta h}{\Delta t}$ is the sea ice growth rate when ice thickness is H (unit: m/s); Ice thickness is the sum of ice growth rate. $\Delta Time$ is the time lag (unit: hour).
The sea ice density and brine volume fraction	$\begin{cases} \rho = \frac{\rho_i F_1(T_i)}{F_1(T_i) - \rho_i S_i F_2(T_i)} \\ f_{vb} = \frac{\rho_i S_i}{F_1(T_i) - \rho_i S_i F_2(T_i)} \end{cases}$ (Cox and Weeks, 1983)	ρ_i=0.917-1.403×10$^{-4}T_i$	ρ is sea ice density (unit: kg/m^3); f_{vb} is the relative brine volume fraction ρ_i is pure ice density (unit: kg/m^3); T_i is the temperature of sea ice (unit: °C); T_a is the air temperature (unit: K); S_i is ice salinity. The functional forms of F_1 and F_2 can be found from the work of Cox and Weeks (1983).
The ice salinity	$\begin{cases} S_i = 14.24 - 19.39H & (H \le 0.4\,\text{m}) \\ S_i = 7.88 - 1.59H & (H > 0.4\,\text{m}) \end{cases}$ (Cox and Weeks, 1983)		H is the ice thickness (unit: m).
The permittivity of sea ice at C-band	$\varepsilon'_{eff} = 3.05 + 0.0072 f_{vb}$ $\varepsilon''_{eff} = 0.02 + 0.0033 f_{vb}$ (Arcone et al., 1986; Vant et al., 1978)		f_{vb} is the relative brine volume fraction.

Table 3. Specifications of the qual-pol RADARSAT-2 SAR data

Scene ID	Date/Time (UTC)	Resolution (m)* Rng × Az	Incidence angle(Deg.)	Beam Mode
#1	19 Mar 2011, 10:25	5.2 × 7.7	29.0	FQ9
#2	19 Mar 2011, 21:51	5.2 × 7.7	42.0	FQ23
#3	19 Mar 2011, 21:51	5.2 × 7.7	42.0	FQ23
#4	20 Mar 2011, 09:56	5.2 × 7.7	49.0	FQ31

*Resolution is nominal. Ground range resolution varies with incidence angle.

Table 4. Specifications of helicopter-borne EMS ice thickness data sets

EM ID	SAR Scene ID coincident with EMS	Date/Time (UTC)	Time difference
P-1	#1	19 Mar 2011 17: 00-17: 20	~ 7 hour
P-2	#2	19 Mar 2011 17: 25-17: 30	~4 hour
P-3	#2	19 Mar 2011 18: 30-18: 45	~3.3 hour
P-4	#3	19 Mar 2011 18: 40-18: 50	~ 3 hour
P-5	#4	20 Mar 2011 11: 55-12: 05	~ 2 hour
P-6	#4	20 Mar 2011 12: 10-12: 25	~ 2.5 hour
P-7	#1	20 Mar 2011 14: 25-14: 30	~ 28 hour
P-8	#1	20 Mar 2011 14: 40-14: 50	~ 28 hour

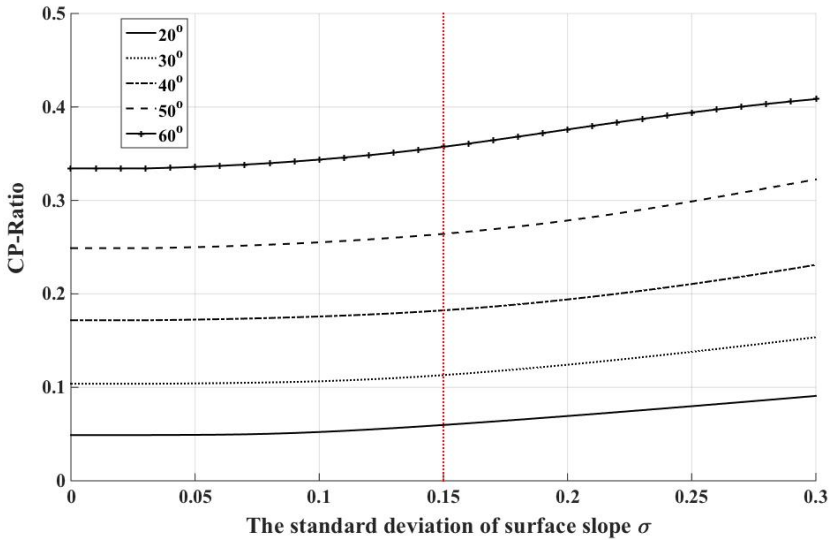

Figure 1. Variations of *CP-Ratio* as a function of the standard deviation of surface slope σ for different incidence angles and ε=3.9+j0.15. The red line marks the maximum threshold of σ for the validity of our approach.

带格式的：对齐网格

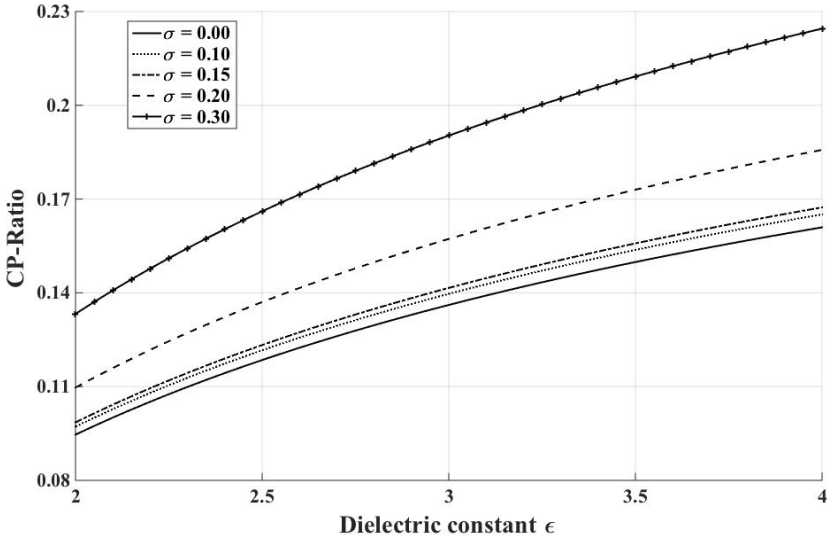

Figure 2. *CP-Ratio* as a function of dielectric constants for different σ and incidence angle=30°. The results for other incidence angles follow the similar trends.

带格式的：左对齐，对齐网格

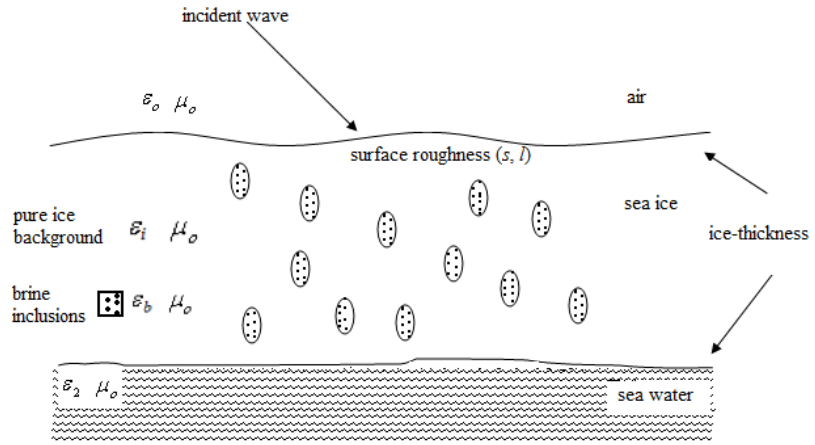

Figure 3. Structure and geometric model of the configuration of sea ice.

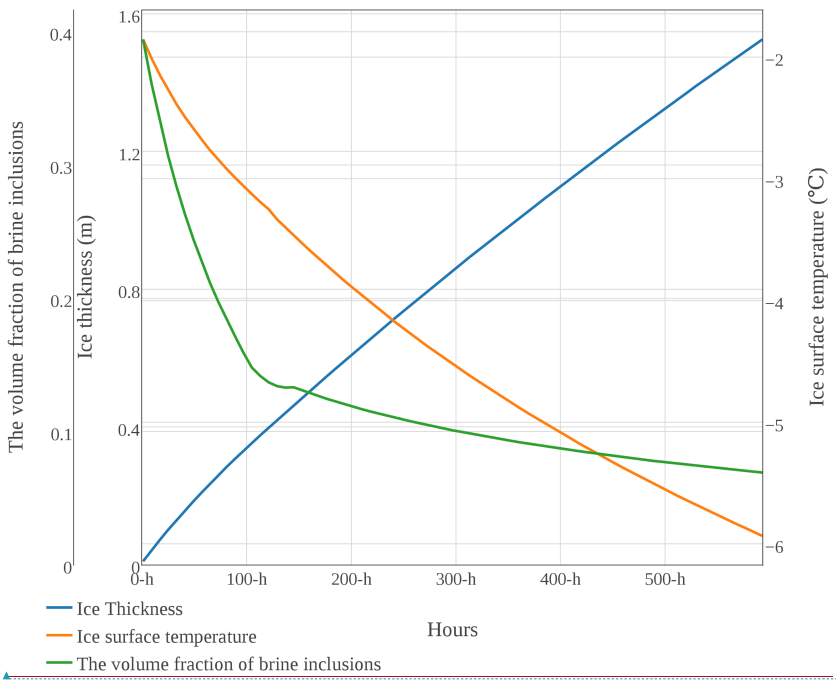

Figure 4. The simulated sea ice growth process. Blue: sea ice thickness; red: sea ice surface temperature; green: the volume fraction of brine inclusions.

带格式的：字体:Times New Roman

带格式的：行距： 单线

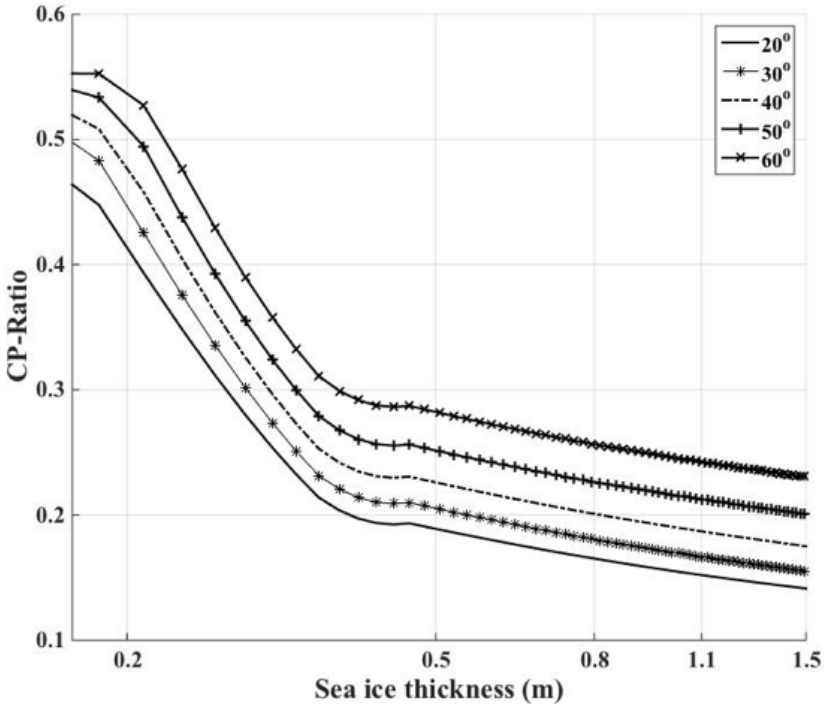

Figure 5. The relationship between *CP-Ratio* and ice thickness at different incidence angles for C-band radar (x-axis in log scale). The incidence angle varies from 20° to 60°. The small-scale roughness parameters are set to s=0.11 cm and l=0.54 cm (case 3), the standard deviation of the surface slope σ=0.1.

带格式的： 行距： 单线

删除的内容: smooth first-year ice

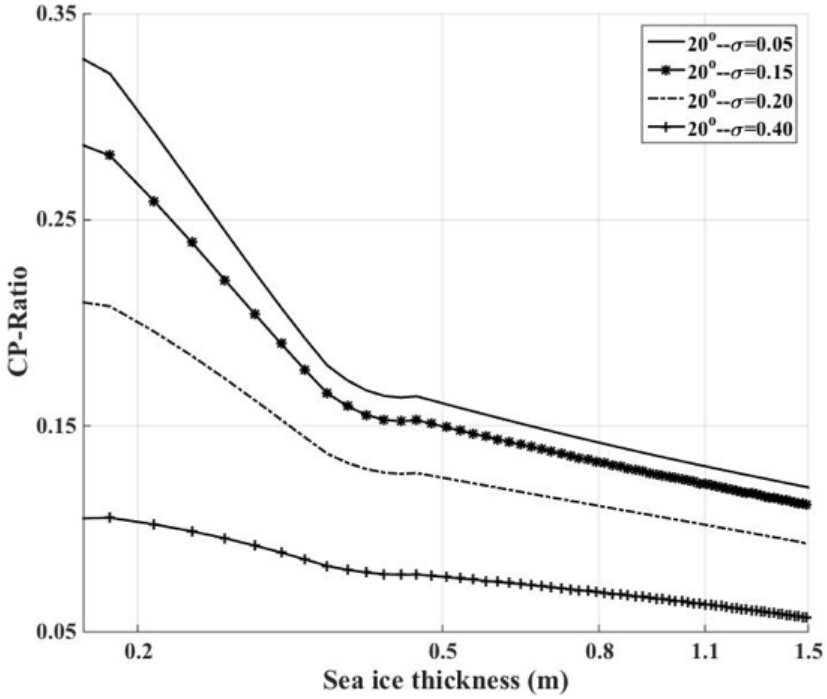
0.35
0.25
0.15
0.05
CP-Ratio
0.2
0.5
0.8
1.1
1.5
Sea ice thickness (m)
20°--σ=0.05
20°--σ=0.15
20°--σ=0.20
20°--σ=0.40

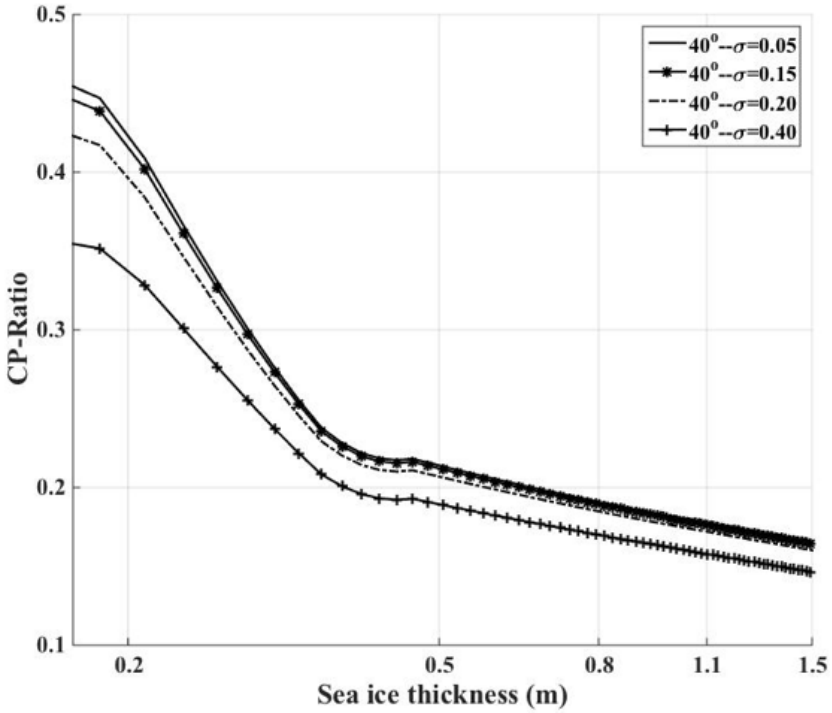

Figure 6. Sensitivity of *CP-Ratio* to the standard deviation of the surface slope σ (x-axis in log scale). The standard deviation of the surface slope σ varies from 0.05 to 0.4, while the small-scale roughness is fixed at s=0.12 cm and l=1.45 cm (case 2). Top figure is for 20° incidence angle and bottom is for 40° incidence angle.

带格式的：行距： 单线

删除的内容: light nilas

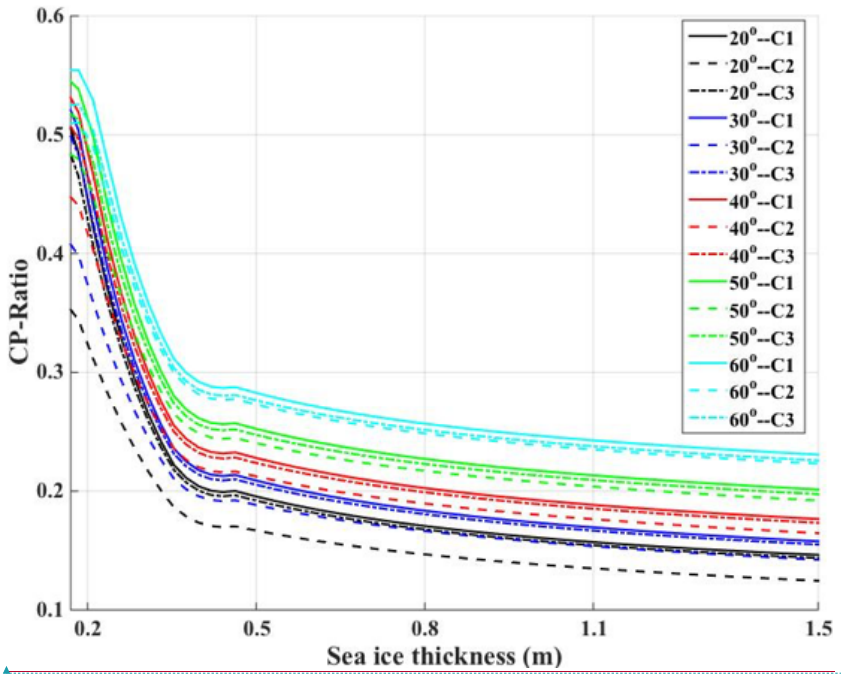

Figure 7. Sensitivity of *CP-Ratio* to the small-scale roughness (x-axis in log scale). The standard deviation of the surface slope σ is fixed at 0.1. Black, blue, red, green and cyan color are for 20°, 30°, 40°, 50°, and 60° incidence angles, respectively. In the legend, C1, C2 and C3 denote the three cases of small-scale surface roughness, respectively (C1: s=0.031 cm, l=1.26 cm; C2: s=0.12 cm, l=1.45 cm; C3: s=0.11 cm l=0.54 cm).

带格式的： 字体:Times New Roman

删除的内容： .

带格式的： 行距： 单线

删除的内容： DN, LN

删除的内容： FI

删除的内容： dark nilas, light nilas and smooth first year ice

删除的内容： .

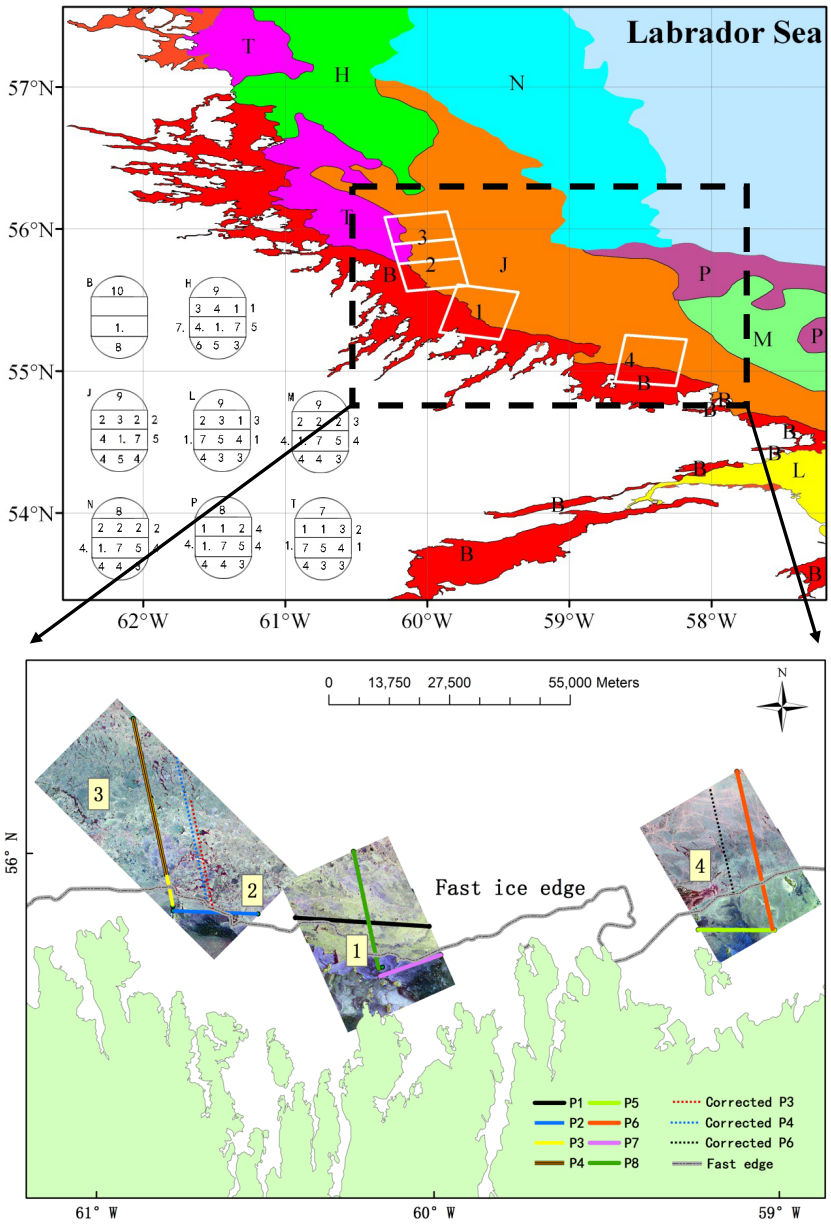

Figure 8. Location of the study site in the Labrador Sea, with Pauli RGB (HH+VV for blue, HH-VV for red, and HV for green) decompositions of the RADARSAT-2 images © MDA. The specifications of the used SAR data are given in Table 3.

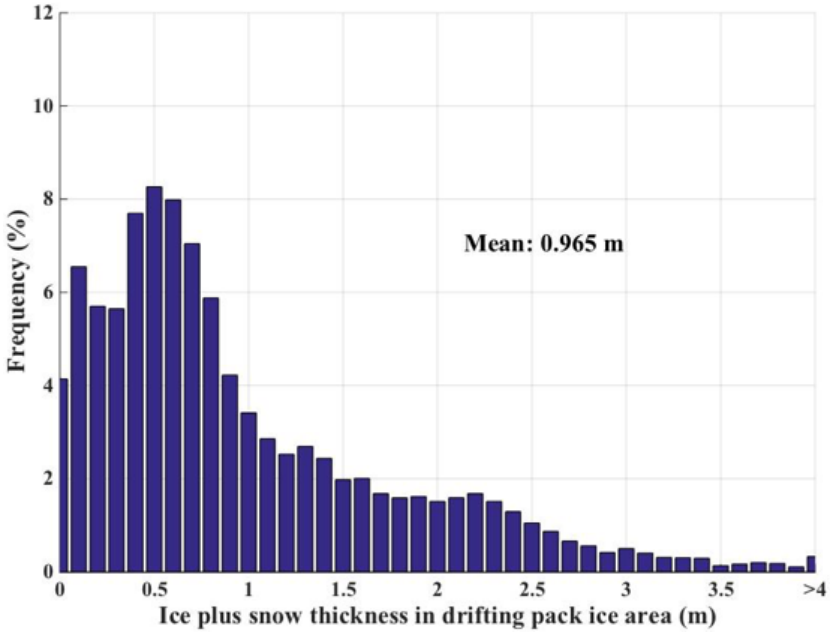
Mean: 0.965 m
Frequency (%)
Ice plus snow thickness in drifting pack ice area (m)
0
2
4
6
8
10
12
0
0.5
1
1.5
2
2.5
3
3.5
>4

(a)

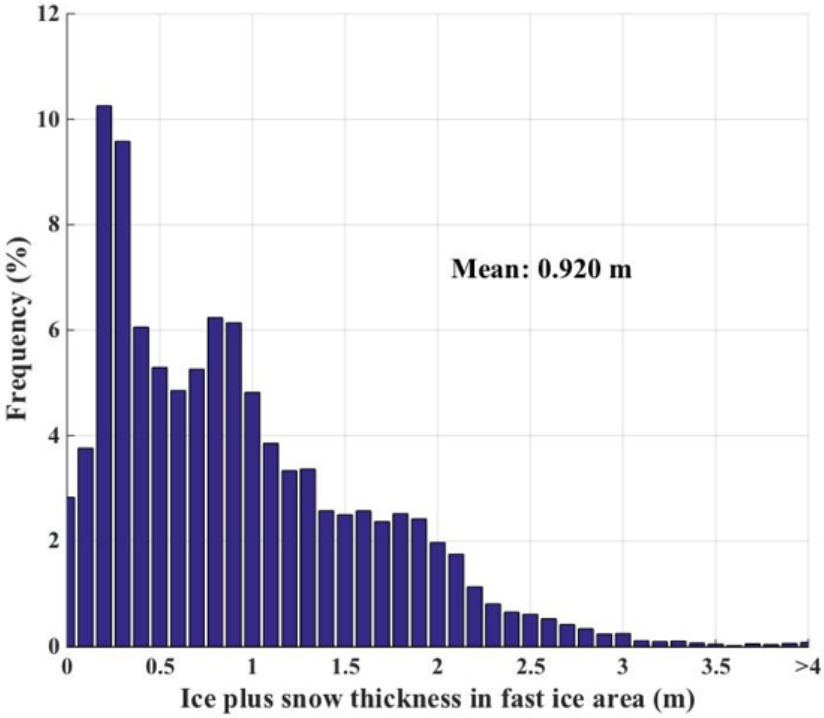
Mean: 0.920 m
Frequency (%)
Ice plus snow thickness in fast ice area (m)
0
2
4
6
8
10
12
0
0.5
1
1.5
2
2.5
3
3.5
>4

(b)

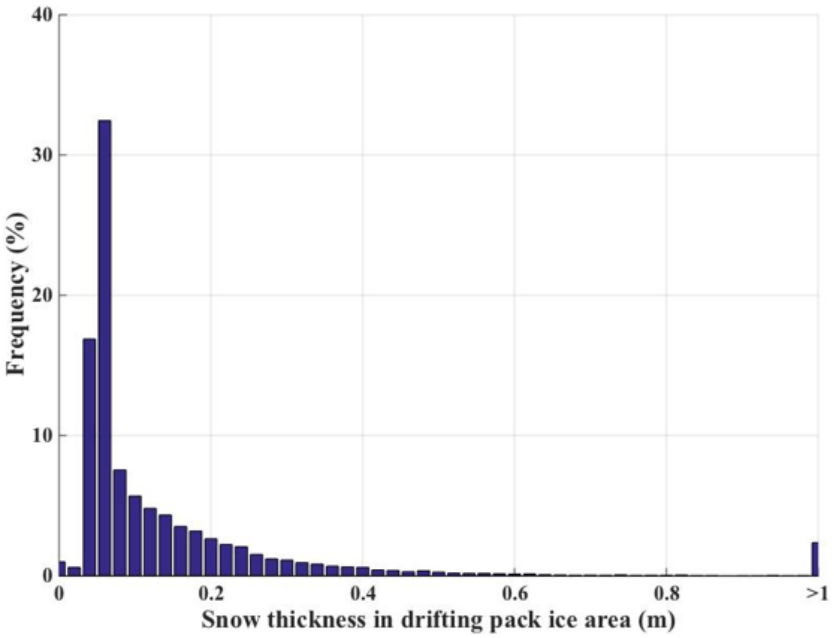
40
30
20
10
0
Frequency (%)
0
0.2
0.4
0.6
0.8
>1
Snow thickness in drifting pack ice area (m)

(c)

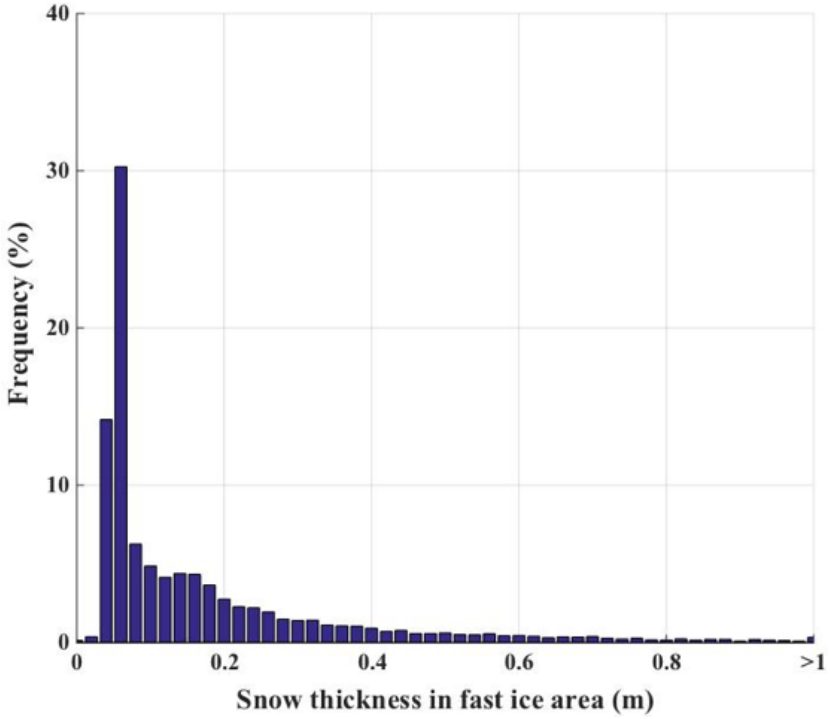

(d)

Figure 9. Histogram of ice and snow thickness in the Labrador Sea. (a) and (b): Ice plus snow thickness collected with EMS in the pack ice (a) and in the fast ice area (b). (c) and (d): Snow thickness collected with GPR in the pack ice (c) and in the fast ice area (d). The bin widths of ice and snow thickness and snow thickness are 0.1 m and 0.02 m respectively. The histograms of the fast ice area are generated from flight tracks of P1, P2, P5, and P7. The histograms of the pack ice area are generated from flight tracks of P3, P4, P6, and P8. These histograms include both level and deformed ice.

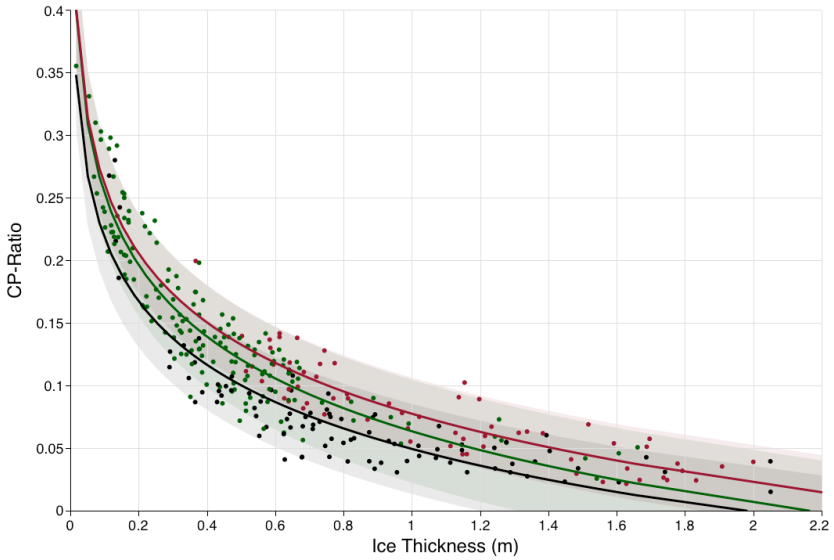

Figure 10. Regressions relating ice thickness to *CP-Ratio* at different incidence angles. The solid lines represent the fits, dashed lines the 90% confidence intervals. The black, green and red colors are used for the incidence angles of 29°, 42° and 49°, respectively.

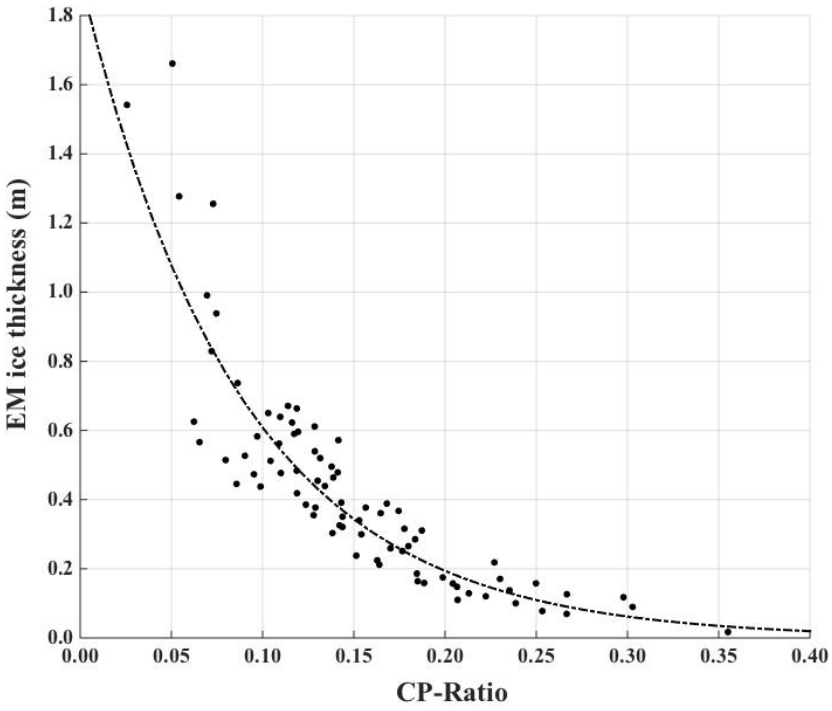
EM ice thickness (m)
CP-Ratio
0.0
0.2
0.4
0.6
0.8
1.0
1.2
1.4
1.6
1.8
0.00
0.05
0.10
0.15
0.20
0.25
0.30
0.35
0.40

(a)

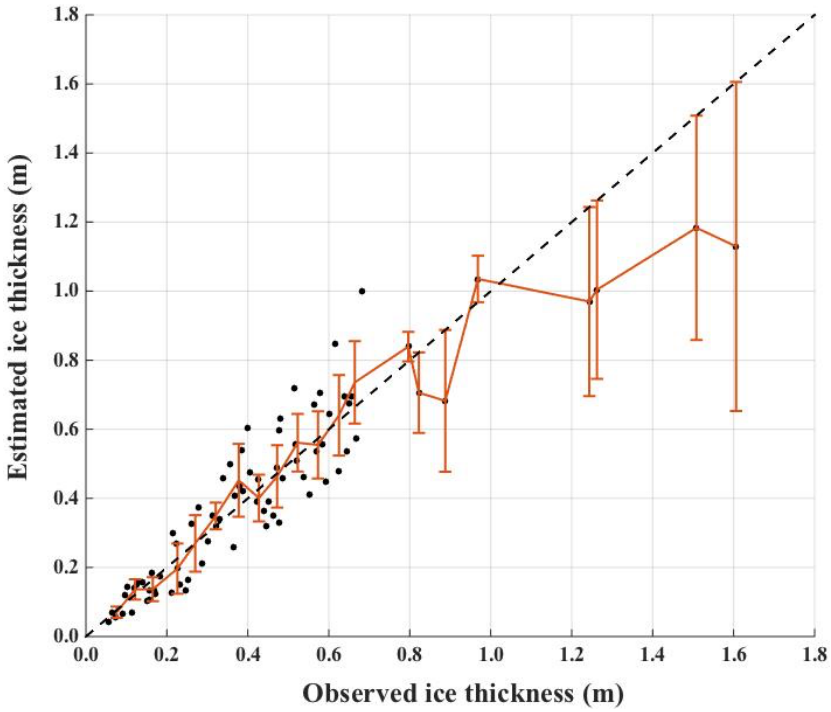

(b)

Figure 11. (a) Relationship between the *CP-Ratio* and the observed EM sea thickness. (b) Comparison between the observed and estimated ice thicknesses, and the errorbars show the standard deviation with respect to the observation data for every 0.05 m segment of ice thickness.

删除的内容: of the plots